

Morphogen gradient scaling by recycling of intracellular Dpp

<https://doi.org/10.1038/s41586-021-04346-w>

Received: 23 April 2020

Accepted: 10 December 2021

Published online: 22 December 2021

 Check for updates

Maria Romanova-Michaelides^{1,4}✉, Zena Hadjivasiliou^{1,2,4}, Daniel Aguilar-Hidalgo^{1,2}, Dimitris Basagiannis¹, Carole Seum¹, Marine Dubois¹, Frank Jülicher^{2,3}✉ & Marcos Gonzalez-Gaitan¹✉

Morphogen gradients are fundamental to establish morphological patterns in developing tissues¹. During development, gradients scale to remain proportional to the size of growing organs^{2,3}. Scaling is a universal gear that adjusts patterns to size in living organisms^{3–8}, but its mechanisms remain unclear. Here, focusing on the Decapentaplegic (Dpp) gradient in the *Drosophila* wing disc, we uncover a cell biological basis behind scaling. From small to large discs, scaling of the Dpp gradient is achieved by increasing the contribution of the internalized Dpp molecules to Dpp transport: to expand the gradient, endocytosed molecules are re-exocytosed to spread extracellularly. To regulate the contribution of endocytosed Dpp to the spreading extracellular pool during tissue growth, it is the Dpp binding rates that are progressively modulated by the extracellular factor Pentagone, which drives scaling. Thus, for some morphogens, evolution may act on endocytic trafficking to regulate the range of the gradient and its scaling, which could allow the adaptation of shape and pattern to different sizes of organs in different species.

Morphogen gradient scaling implies the regulation of the gradient range (that is, its decay length) to remain proportional to tissue size^{9,10}. In the case of the Dpp morphogen gradient, to understand how the decay length is regulated during scaling, it is essential to determine which cellular transport phenomena are important during Dpp gradient formation and which of these change as the tissue grows. Those phenomena could include the extracellular diffusivity of Dpp and the recycling of internalized morphogen molecules, however, the relative contribution of these has been a subject of debate^{8,11–13} (for a discussion of this debate, see Supplementary Information section 4.2).

Photoconversion assay and Dpp recycling

We first developed an assay to address whether internalized Dpp molecules can contribute to the formation of the gradient. We generated anti-GFP nanobodies (GFP-binding protein, GBP) fused to a photoconvertible protein, Dendra2 (GBP–Dendra2). GFP–Dpp-expressing wing discs were incubated with GBP–Dendra2, which binds extracellular GFP–Dpp. GBP–Dendra2 then follows GFP–Dpp through the endocytic pathway. We then removed extracellular GBP–Dendra2 bound to Dpp by a quick acid wash at 4 °C, leaving only the endocytosed molecules. Photoconversion of this intracellular GFP–Dpp-bound GBP–Dendra2 in a region of interest (ROI) (whether in the target (Fig. 1a) or source tissue (Fig. 1b)) allows us to address whether these internalized molecules can move to neighbour cells and form a gradient there (for details and controls of this assay, see Supplementary Information section 2.8, Extended Data Fig. 1a–d, e–j).

Figure 1a–c shows that, in late discs, such a gradient is formed. Because the photoconverted molecules were only in the endocytic pathway, this result indicates that internalized Dpp molecules can

be recycled to spread into the target tissue (see also Supplementary Video 1). Photoconversion not only in the source territory (Fig. 1b), but also in the target territory led to the formation of a gradient (Fig. 1a), confirming that Dpp molecules can also be re-exocytosed from the target cells. The photoconversion experiment suggests that recycling could contribute to some extent to gradient formation and might in principle underlie scaling. To study the relevance of recycling in scaling, we measure the cellular trafficking rates of Dpp during the formation of the gradient as the tissue grows.

Key Dpp transport steps

We focused on cells in the posterior compartment of the wing imaginal disc, as this compartment is exclusively composed of target cells that do not produce Dpp themselves^{14–16}. We distinguish five pools of Dpp and consider trafficking through these pools mediated by eight different transport steps (Fig. 1d). A pool of unbound extracellular molecules with concentration L diffuses with extracellular diffusivity D_0 . Unbound molecules bind to receptors at rate k_{on} to become part of the bound pools S_L and S_R on the left and right surfaces of cells of size a . Bound molecules return to the extracellular pool by unbinding from the receptors (k_{off}). Bound to these receptors, they are internalized with an endocytosis rate k to fill an endosomal pool S_e . This pool S_e is emptied through three pathways: recycling back to the plasma membrane at rate k_r , degradation at rate k_1 and transfer at rate k_i to another pool (S_i) from where it cannot be recycled, but only degraded at rate k_2 . This immobile pool, S_i , is motivated by the existence of an immobile fraction in fluorescence recovery after photobleaching (FRAP) experiments¹². We define an effective degradation rate $k_o = k_1 + k_i$, which represents the irreversible output from the mobile pool.

¹Department of Biochemistry, Faculty of Sciences, University of Geneva, Geneva, Switzerland. ²Max Planck Institute for the Physics of Complex Systems, Dresden, Germany. ³Cluster of Excellence Physics of Life, TU Dresden, 01307 Dresden, Germany. ⁴These authors contributed equally: Maria Romanova-Michaelides, Zena Hadjivasiliou. ✉e-mail: maria.romanova@unige.ch; julicher@pks.mpg.de; marcos.gonzalez@unige.ch

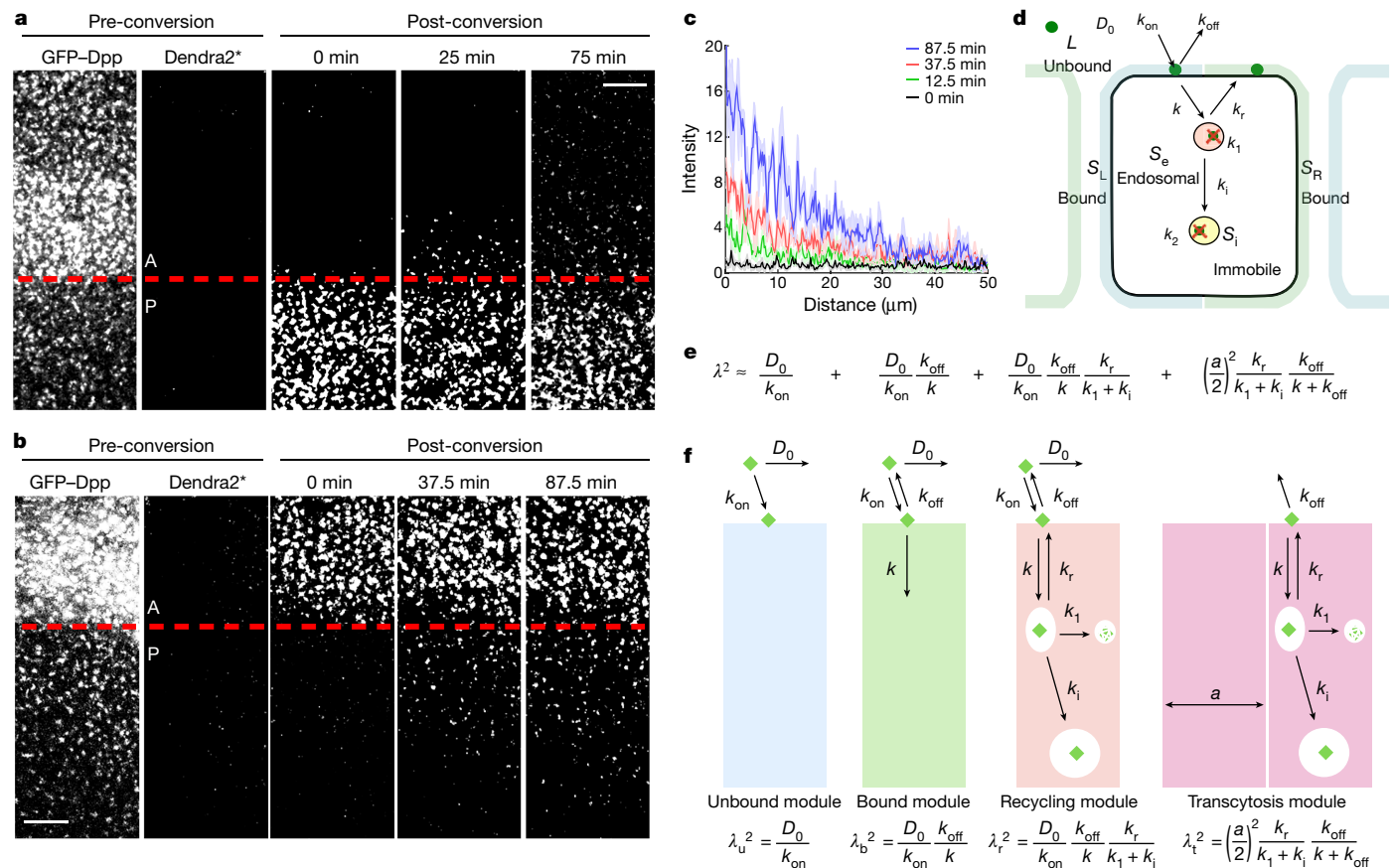


Fig. 1 | Recycling contributes to gradient formation: photoconversion assay, Dpp transport steps and modules of transports. **a–c.** Photoconversion assay. **a, b.** Confocal images of eGFP-Dpp^{LOP} and photoconverted GBP-Dendra2 (Dendra2*) before (pre-conversion). Dendra2* is also shown at different times after photoconversion (post-conversion) in the posterior (P) compartment (**a**) and in the anterior (A) compartment (**b**). Before conversion, after pulse-chase and acid wash, only internalized GBP-Dendra2 remains. Photoconversion, below (**a**) and above (**b**) the dotted red line. Note the build-up of a Dendra2* gradient outside the photoconverted region. Scale bars, 10 μm. *n* = 3 and *n* = 7 biologically independent samples for **a** and **b**,

This description is equanimous: depending on parameter values, the same general description allows us to capture a wide variety of transport models. For example, within this description, the recycling rate or the unbinding rate might be negligible, leading to a scenario in which only extracellular molecules may contribute to the formation of the gradient (for examples of extreme scenarios, see Extended Data Fig. 1k–n, Supplementary Information section 4.2.2).

It is important to note that certain scenarios of transport that have been proposed—such as transport via long or monodirectional cytonemes^{17–19}—are not captured in our description. Furthermore, unbound ligand molecules could in principle leak out of the epithelium, as recently studied in a synthetic system in which secreted GFP binds to a membrane nanobody and forms gradients¹³. We have investigated experimentally and theoretically the potential role of leakage in our system using a GFP construct that is transcribed, translated, cleaved and trafficked like Dpp. This suggests that for molecules processed and secreted in the epithelium like Dpp, leakage is unlikely to be important (Extended Data Fig. 2a–j; see further considerations in Supplementary Information sections 2.11, 3.10, 4.3).

Our description of Dpp transport can be captured by a set of dynamic equations that describe the time evolution and the spatial distribution of Dpp in the five pools for given values of the transport rates²⁰

respectively. **c.** Average spatial distribution of GBP-Dendra2* fluorescence signal as a function of the distance to the source boundary (dotted red line in **b**) at different times after photoconversion at the source (**b**). Shaded areas, s.e.m.; *n* = 7 biologically independent samples. **d.** Scheme of five pools and eight transport rates of morphogen transport. **e.** λ^2 as a function of Dpp transport rates. λ , decay length. **f.** Scheme of the four modules of Dpp transport defined by the terms in the λ^2 equation. Bottom, expression of each of the four modules ($\lambda_u^2, \lambda_b^2, \lambda_r^2, \lambda_t^2$); $\lambda^2 = \lambda_u^2 + \lambda_b^2 + \lambda_r^2 + \lambda_t^2$. For genotypes in figures, see Supplementary Tables 1, 2.

(Supplementary Information section 1.1). From these equations, we obtain an expression for the decay length λ of the gradient in steady state, as a function of the transport rates:

$$\lambda^2 \approx \frac{D_0}{k_{on}} \left(1 + \frac{k_{off}}{k} \left(1 + \frac{k_r}{k_i + k_1} \right) \right) + a^2 \frac{k_r}{4(k_i + k_1)} \frac{k_{off}}{(k_{off} + k)} \quad (1)$$

In Supplementary Information sections 2.9, 2.10, 3.9, Extended Data Fig. 2k–s, we show how this expression holds during scaling, when the system is only in quasi steady state, as previously discussed⁶.

Four transport modules in gradient formation

Equation (1) for λ^2 contains four terms that reflect four modules of Dpp transport (see four terms in Fig. 1e, f, Supplementary Information section 3.1). The first term ('unbound module'; Fig. 1f) considers the extracellular unbound molecules, their extracellular diffusivity and binding to membrane receptors. The second term ('bound module') considers in addition the bound molecules, which can unbind and thereby contribute to the diffusing unbound pool. Internalization by endocytosis eliminates the possibility that some of these bound molecules are transferred to the unbound pool. The third term ('recycling module') considers the endosomal molecules, which can be recycled

to the plasma membrane, where they can again unbind to contribute to the diffusing unbound pool. This process is counteracted by endosomal degradation or immobilization. Note that the recycling module is not equivalent to the recycling rate, as it depends on all the transport rates, except k_2 . Notably, extracellular diffusivity and the binding rate are essential for the three modules described above.

Finally, the fourth term reflects a 'transcytosis module' that does not depend on extracellular diffusivity, but depends on the cell size, α . This fourth term describes the movement of molecules throughout the tissue by unbinding from one cell and binding to the adjacent neighbour cell without extracellular diffusion, in a 'bucket brigade'-like process²¹ in which the ligand is handed directly from receptor to receptor between neighbour cells.

Estimation of Dpp transport rates

The relative importance of each module for λ^2 defines the regime of Dpp transport and depends on the eight transport rates. Therefore, to characterize the regime of transport, we developed five assays to measure these rates (for in-depth descriptions of the parameterization assays see Supplementary Information sections 2.1–2.5). We used the LexA/LOP system to express eGFP-tagged Dpp at quasi-endogenous levels (eGFP-Dpp^{LOP} (ref. 22) (see Methods, Extended Data Fig. 3a–d).

The assays quantify independent dynamic properties of the system or properties of its steady state: (i) the steady-state decay length (Fig. 2a, Extended Data Fig. 3e–j; see Supplementary Information section 2.1); (ii) dynamics of internalization of extracellular Dpp molecules by using nanobodies (Fig. 2b–f, Extended Data Fig. 3k–v, Supplementary Information section 2.2); (iii) FRAP in target tissues in a new primary culture system (Extended Data Fig. 4a, b, Supplementary Information section 2.5), which confirms and extends previous FRAP analysis^{3,12} (for detailed comparison see Supplementary Information sections 3.3, 3.4, Extended Data Fig. 4c–f); (iv) determination of the fraction of extracellular molecules by calibrating nanobodies (Fig. 2g, Extended Data Fig. 4g–i, Supplementary Information section 2.3); and (v) dynamics of the immobile fraction by a long-term FRAP assay (Extended Data Fig. 2k–n, Supplementary Information section 2.4). Each of these assays depends on most transport rates. We therefore perform a sequence of data analysis steps using the assays, in which each assay adds further constraints to the parameter values.

In brief, in this sequence of steps, we first fit the dynamics of the nanobody assay to our theoretical framework (Supplementary Information section 2.2.1). This yields narrow confidence intervals for the recycling rate k_r , an effective internalization rate $k_N = k(\frac{k_{on}}{k_{on} + k_{off}})$ and the effective degradation rate k_o (Supplementary Information section 2.2.3). Second, we use equation (1) and the measured confidence interval of the decay length to constrain the values of D_o , k_{on} , k_{off} . Third, we use an approximate Bayesian computation approach to infer posterior distributions for D_o , k_{on} , k_{off} , k_i and k_1 . For this procedure, we sample large sets (around 10^7 sets) of parameter values for which we numerically solve the equations that describe Dpp transport under the FRAP assay conditions (Supplementary Information section 1.1), and quantify the similarity between calculated recoveries and the experimental FRAP recovery profiles (Supplementary Information section 2.5.2). This provides narrow ranges for the values of D_o , k_{on} , k_{off} , k_i and k_1 (Extended Data Fig. 4j). Fourth, we further restrict the ranges for the parameters D_o , k_{on} , k_{off} , k_i and k_1 by (i) excluding parameter sets that are inconsistent with the measured extracellular fraction (Supplementary Information section 2.5.2, Extended Data Fig. 4k–m) and (ii) using the measured value of k_2 obtained from the long-term FRAP assay (Supplementary Information section 2.4, Extended Data Fig. 2k–n). The numerical C++ code and the Wolfram Mathematica scripts for this procedure are available online.

Using this procedure, we obtained a compact cluster of value sets for the eight parameters (see Fig. 3a (orange) for large discs with posterior compartment length $l = 144 \pm 4 \mu\text{m}$; Extended Data Fig. 4k). The spread

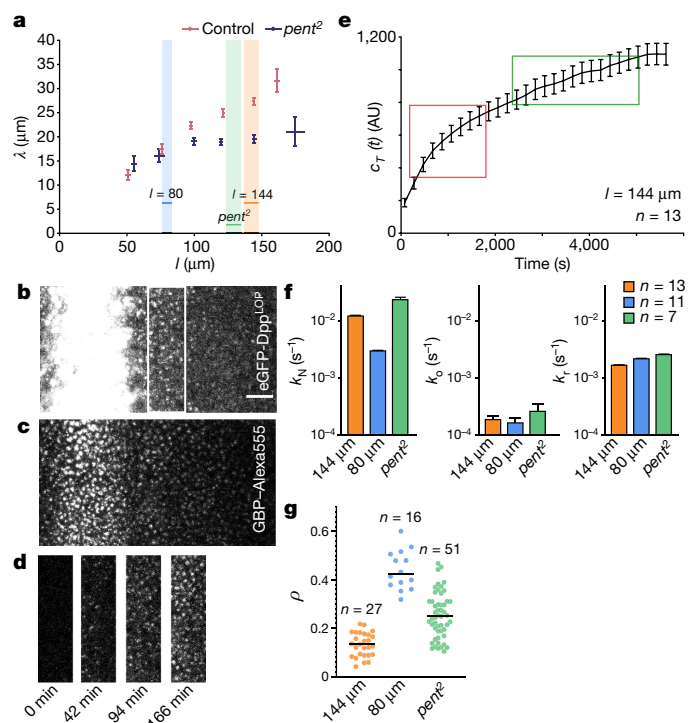


Fig. 2 | Parameterization assays. **a**, Decay length λ of the eGFP-Dpp^{LOP} gradient versus the posterior compartment length l for control ($n = 157$) and $pent^2$ ($n = 63$) discs. See also Extended Data Fig. 3j. Shaded areas, range of l in three experimental conditions: eGFP-Dpp^{LOP} control discs, $l = 144 \pm 4 \mu\text{m}$ and $l = 79.3 \pm 1.4 \mu\text{m}$ mean posterior length; $pent^2$, $l = 129.8 \pm 4.9 \mu\text{m}$ mean length. **b–f**, Nanobody internalization assay. **b**, Confocal images of the eGFP-Dpp^{LOP} gradient (**b**), and internalized GBP-Alexa555 (**c**) after 94 min of incubation with the nanobody. Scale bar, $10 \mu\text{m}$. **d**, GBP-Alexa555 signal in the ROI indicated in **b** at different times of nanobody incubation. **e**, Average dynamics of the GBP-Alexa555 fluorescence signal in the ROI in $l = 144 \mu\text{m}$ discs (for the other conditions see Extended Data Fig. 3l). $n = 13$ biologically independent samples. Data represented as mean values \pm s.e.m. AU, arbitrary units. Note the exponential dynamics (red box) and linear dynamics (green box), which dominate early and late, respectively, and emerge from the trafficking rates described in Extended Data Fig. 3m. For details see Supplementary Information section 2.2.1. **f**, Estimated k_N , k_o and k_i in the three conditions described in **a**. Data are represented as values determined by simultaneous fitting of $n = 13$, 11 and 7 independent uptake curves \pm confidence interval of the fit. **g**, Extracellular fraction in control discs of $l = 144 \mu\text{m}$ and $l = 80 \mu\text{m}$ and in $pent^2$ mutant discs. Center values, means. Bars (**a**, **b**), s.e.m.; n , number of biologically independent samples (**e**, **f**, **g**).

of this cluster corresponds to the precision of the different parameter values. This spread is constrained by the fact that each parameter value set (that is, each point in the cluster) is consistent with all five assays. It should be noted that the precision of parameter estimation is dependent on the quality of measurements performed with each assay (see Fig. 2f, g, Extended Data Figs. 3e, g, k, 4b–d, Supplementary Information section 2.5.1 for an evaluation of the precision of our assays). To address this, we studied how robust the position and spread of the cluster are when we consider a higher imprecision than the one obtained in key assays such as the extracellular fraction assay or the FRAP assay. To this end, we simulated a relaxation in the precision of the assays in our numerical analysis (Extended Data Fig. 5a, b, Supplementary Information section 3.7). We found that the position and spread of the clusters remained largely unchanged when we considered values beyond the uncertainty range characteristic of these experimental assays. Despite the experimental imprecision (and even when relaxing it further), our parameterization approach yields robust parameter estimates.

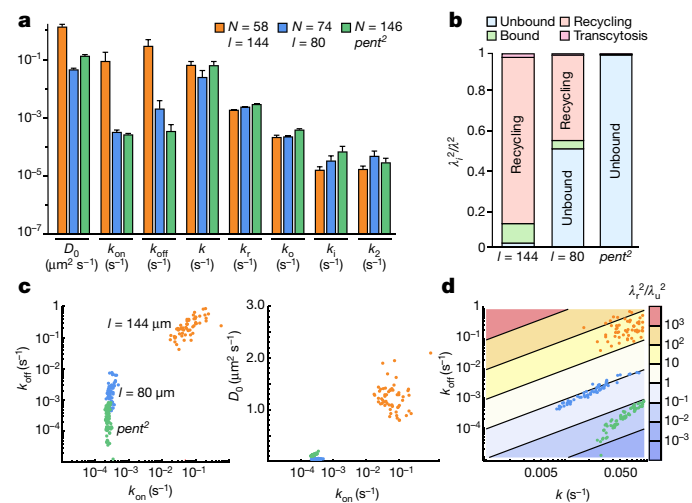


Fig. 3 | Parameterization of Dpp transport rates. **a**, Average estimated parameters in the three experimental conditions. Data represented as mean values. Bars, s.d.; *N*, number of sets of values returned by the approximate Bayesian computation. **b**, Stacked bar chart showing the relative contribution of the different modules to λ^2 (described in Fig. 1e, f). **c**, **d**, Sets of parameter values returned by the approximate Bayesian computation, which satisfy constraints given by all experimental assays. Values are projected in (k_{on}, k_{off}) and (D_0, k_{on}) (**c**) and (k, k_{off}) (**d**) planes. In **d**, the calculated isolines of the theoretical ratios of the recycling to the unbound module $(\lambda_u^2/\lambda_u^2)$ are shown in different colors. These isolines indicate the relative contribution of recycling and unbound modules to Dpp transport. Note that the three experimental clusters (large, small and *pent*² discs) are separated by isolines that define three different regimes: dominating unbound module (*pent*²), combined unbound and recycling module (small discs) and dominating recycling module (large).

Figure 3c, d shows the cluster of value sets determined using this procedure and projected on different parameter planes, for the pairs (k_{on}, k_{off}) , (k_{on}, D_0) and (k, k_{off}) (see also Extended Data Fig. 4I). It should be noted that some parameters are inferred by our Bayesian approach and are not obtained through direct measurement; for example, k_{on}, k_{off} . However, given that our model framework is broad and the parameterization is supported by five independent quantitative assays, our approach provides parameter value estimates with a narrow level of uncertainty, within an order of magnitude (Fig. 3a, c, d, Extended Data Fig. 4I, m, Extended Data Tables 1, 2).

In large discs, with posterior compartment length $l = 144 \pm 4 \mu\text{m}$, unbound Dpp molecules move extracellularly with a diffusivity $D_0 \approx 1.2 \mu\text{m}^2 \text{s}^{-1}$ dwelling 5.6 s per cell. Unbound molecules bind with a rate $k_{on} = (0.02-0.6) \text{s}^{-1}$: free molecules remain unbound more than 2 s before binding. Bound molecules unbind with a rate $k_{off} = (0.04-0.9) \text{s}^{-1}$. The values of k, k_i and k_o measured here agree with previous reports²³⁻³⁰ in mammalian cultured cells (Extended Data Table 1). By contrast, considering the known unbinding rates of BMP2 and BMP4 from the receptor^{24,31}, the value we obtained for k_{off} was high (Fig. 3a, c).

Tkv is not the internalization receptor

With the estimated k_{off} values, bound molecules in the plasma membrane remain attached less than 25 s before they detach. Previous reports in mammals showed that the rate k_{off} of the type I BMP receptor for its BMP2 ligand corresponds to about 800 s (ref. 24). This suggests that the fly BMP2 and BMP4 receptor Thickveins (Tkv) is not the receptor that internalizes Dpp in the wing disc. To challenge this hypothesis, we performed a nanobody internalization experiment in GFP-Dpp-expressing flies containing null mutant clones for Tkv (*brk*^{M68} *tkv*⁸ see Methods, Fig. 4a, b).

Internalization of eGFP-Dpp is normal in *tkv* mutant cells (Fig. 4a, b) and the mutant clones do not affect the gradient profile, consistent with previous reports³². Therefore, the receptor that internalizes Dpp is not its signalling receptor Tkv, but a different one with a higher k_{off} value (see Supplementary Information sections 4.4, 4.5 for details). To signal, Dpp possibly encounters and binds Tkv in an intracellular compartment from which molecules do not return to the unbound extracellular pool, akin to the immobile pool. A similar scenario has been proposed for Wingless and its signalling receptor Frizzled in the wing³³.

Gradient formation by recycling module

To characterize the Dpp transport regime in large discs, we estimate the contributions of the four transport modules from equation (1) using the measured parameter values (Supplementary Information section 3.1). A particular regime is characterized by the prevalence of one or several transport modules over others. Examples of regimes include scenarios in which the unbound module, the transcytosis module or the recycling module prevail (Supplementary Information section 4.2.2). Scenarios with mixed modules are also possible. The relative contribution of a module depends in turn on the actual values of the transport rates (see above). It is worth noting that this approach is equanimous: depending on parameter values, the same general description allows a wide variety of transport regimes to be captured (Fig. 1e, f, Extended Data Fig. 1k); that is, the actual regime emerges from the set of rate values determined experimentally in our approach (Fig. 3a, Extended Data Table 1). Therefore, a regime is not a consequence of particular modelling assumptions, but emerges from parameter values determined experimentally.

With the transport parameter values that we obtained, the recycling module contributes to about 90% of λ^2 , whereas the other modules are negligible (Fig. 3b). Therefore, Dpp transport is characterized by a ‘combined transport regime’, in which extracellular diffusivity, recycling and unbinding are at the basis of gradient formation (Extended Data Fig. 5c-e, Supplementary Information section 3.5). This regime is distinct from pure transcytosis²¹, which is captured by the transcytosis module and does not require extracellular diffusivity (see Supplementary Information section 4.2, Extended Data Fig. 1k-n). Instead, in the Dpp transport regime found in the wing, recycling and extracellular diffusivity are both key. Recycling mobilizes intracellular molecules to the diffusing extracellular pool to form the gradient, consistent with the result of the photoconversion experiment (Fig. 1a, b).

This combined transport regime that we found in the wing is also different to other regimes described in the literature^{13,34}, which are dominated by the extracellular diffusion of the unbound pool (captured by the unbound module; Extended Data Fig. 1k). In the regimes in which the diffusion of the unbound pool dominates transport, morphogen concentration decays as a gradient by means of morphogen capture through irreversible receptor binding³⁴ and/or leakage of the morphogen out of the epithelium¹³. Indeed, to investigate the minimal requirements for gradient formation, recent work has showed that GFP by itself can form a diffusion-based gradient when binding to membrane-associated anti-GFP antibodies, which also limits leakage¹³. In this type of regime, intracellular trafficking and the recycling module are irrelevant, in contrast to the ‘combined transport regime’, in which leakage is not important, but intracellular trafficking and the recycling module are.

Recycled Dpp spreads in the tissue

A regime of combined transport is characterized by non-negligible recycling and unbinding rates. We developed three further independent assays to test whether this applies to the wing. These are independent falsification assays that challenge our conclusions. In an internalized FRAP (iFRAP) assay, we assess quantitatively the capacity of internalized molecules to be recycled, to unbind and to move to neighbour cells (Fig. 4c, d, g). Similar to the photoconversion experiment, we label

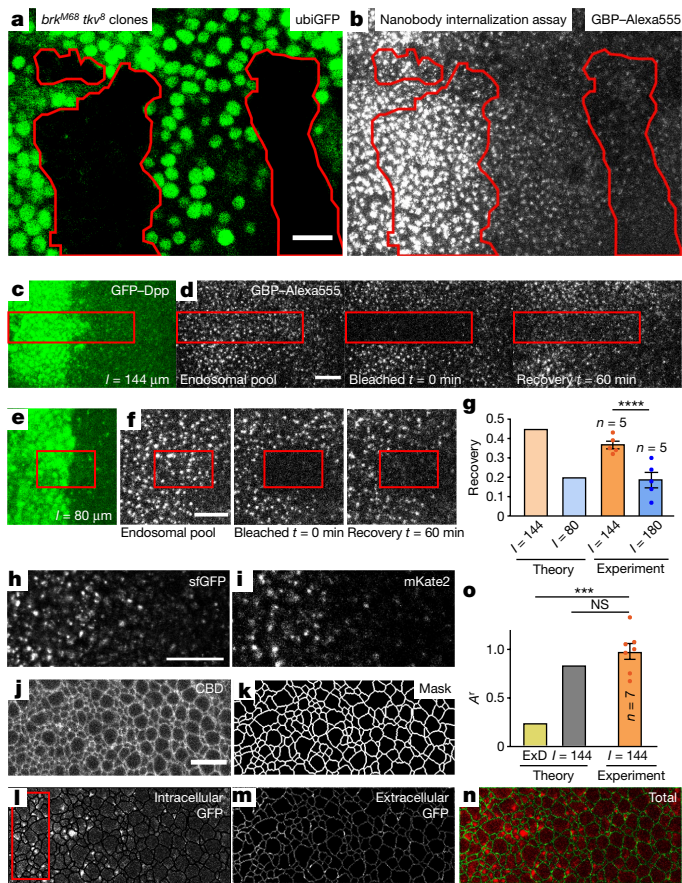


Fig. 4 | Internalized Dpp is recycled and spreads. **a, b**, Nanobody internalization assay in eGFP-Dpp^{Gal4} discs containing *brk^{M68} tkv⁸* clones marked by absence of ubiGFP (**a**). Internalized GBP-Alexa555 (**b**) after 50-min nanobody incubation. **c–g**, iFRAP assay. Confocal images of eGFP-Dpp^{L^{OP}} (**c, e**) and GBP-Alexa555 (**d, f**) after 30-min nanobody incubation and acid wash ('endosomal pool'), after bleaching of the Alexa555 signal ($t = 0$ min) and 60 min after bleaching ($t = 60$ min). **c, d**, $l = 144 \mu\text{m}$; **e, f**, $l = 80 \mu\text{m}$. **g**, Percentage of Alexa555 fluorescence recovery 30 min after photobleaching ('experiment'), compared with the corresponding values calculated numerically ('theory') using experimental parameter values in Extended Data Table 1. **h–o**, Dpp^{Timer} assay. **h–j**, Confocal images of the Dpp^{Timer} gradient (**h**, sfGFP; **i**, mKate2; and **j**, extracellular Cascade Blue dextran (CBD)). **k**, Outline of cells based on CBD signal. **l, m**, sfGFP intracellular (**l**) and extracellular (**m**) pools defined using **k**. **n**, Merge. **o**, Age ratio (A') considering the red box in **l**. Theoretical A' ('theory') was calculated numerically using the set of values in Extended Data Table 1 and Extended Data Fig. 11 for ExD (consistent with a previous report¹⁷) and the set of parameterized values in Fig. 3a and Extended Data Table 1 for $l = 144 \mu\text{m}$. Third bar ($l = 144 \mu\text{m}$; 'experiment'), average A' determined experimentally. P values: 0.000019, **** (**g**); 0.1310, NS (**o**, comparing $l = 144 \mu\text{m}$ theory and experiment); 0.0001, *** (**o**, comparing ExD theory and $l = 144 \mu\text{m}$ experiment). NS, not significant. Two-tailed two sample t-test. Bars, s.e.m.; n , sample size. Scale bars, 10 μm (**a, d, f, j**).

internalized eGFP-Dpp molecules with GBP-Alexa555. We then bleach the Alexa555 fluorescence in a ROI and follow the recovery of fluorescence in the ROI (for details and controls on the experiment, see Supplementary Information section 2.7, Extended Data Figs. 1e–j, 5f–h). The recovered Alexa555 fluorescence corresponds to the intracellular GBP-Alexa555-bound eGFP-Dpp molecules that were re-exocytosed and moved from surrounding neighbour cells into the bleached ROI. Fluorescence intensity in the bleached ROI recovers by 37% within 30 min (Fig. 4c, d, g). This is consistent with the theoretical expectation for iFRAP using the parameter values estimated with our assays (Fig. 4g, Extended Data Table 1 and Extended Data Fig. 5i). Therefore,

intracellular molecules are recycled and reappear in neighbour cells, consistent with the photoconversion experiment (Fig. 1a, b).

A Dpp^{Timer} experiment further validates this result (Fig. 4h–o). We generated a 'timer' transgene³⁵: Dpp fused to both a fast maturing GFP (sfGFP; ref. 35) and a slow maturing, red mKate2 (ref. 36). Young Dpp molecules are only green, whereas older Dpp molecules are both green and red (for details and controls on the experiment, see Supplementary Information section 2.6, Extended Data Fig. 6a–j). We define the 'age' of Dpp molecules A as the fraction of red over green signal ($A = [\text{red}]/[\text{green}]$). As molecules move away from the source, they become older: A increases (see Supplementary Information section 2.6). We finally define A' as the ratio between the ages of molecules in the extracellular and intracellular compartment ($A' = A_{\text{ext}}/A_{\text{int}}$). Note that a low pH affects the fluorescence signal of the two fluorophores to a very similar extent (Extended Data Fig. 6h–j), which precludes issues when using the timer also in the acidic pH of endosomes.

If intracellular molecules do not return to the extracellular space (no recycling), extracellular molecules must be young (green, not red), whereas intracellular molecules will be older (green + red; $A' \approx 0$). This scenario corresponds to a regime of transport in which the gradient is formed by extracellular diffusion (ExD) as previously considered³⁴. Conversely, when the recycling rate is important, the age of intracellular and extracellular molecules would be comparable ($A' \approx 1$).

In our experiment, the measured Dpp^{Timer} ages in the extracellular and intracellular space are similar ($A' \approx 1$; Fig. 4o), consistent with the theoretical expectation using rate values obtained with our assays, including a high k_{off} value. This confirms that the intra- and extracellular pools exchange, implying that recycling is important. Both falsification assays validate our parameterization of rate values and exclude the theoretical extreme ExD regime³⁴ in these late discs.

To further investigate the role of recycling in gradient formation and scaling, we look at the effect on the Dpp gradient of impaired endocytic recycling. To interfere with Dpp recycling, we silenced by RNA interference (RNAi) in the target tissue the two canonic recycling Rab proteins: Rab11 and Rab4 (ref. 37) (Extended Data Fig. 6k–o, Supplementary Information section 2.12). Indeed, after downregulation of Rab4 and Rab11, the Dpp recycling rate is decreased, and, correspondingly, Dpp gradients shorten significantly (Extended Data Fig. 6m–o). Note that downregulation of Rab4 and Rab11 could affect the trafficking of other membrane components of the pathway (including Dpp receptors, heparan sulfate proteoglycan (HSPG) factors and so on). The effect of this downregulation on recycling of Dpp in this case might be indirectly explained through trafficking defects of these components.

Discs with downregulated Rab4 protein present a scaling phenotype: in discs of increasing size, the gradient remains short (Extended Data Fig. 6m). This indicates that recycling has a central role in gradient formation and scaling: a recycling mutant is a scaling mutant.

Scaling by recycling

During growth, the decay length of the Dpp gradient increases to stay proportional to the size of the organ³ (Fig. 2a, Extended Data Figs. 3j, 6p–r). Gradient scaling must be mediated by changes in transport rates. Indeed, small ($l = 80 \mu\text{m}$) and large discs show clusters of parameter values that are clearly different (Fig. 3c, d). The two clusters are set apart by the values of D_0 , k_{on} and k_{off} (Fig. 3a, c, d), which are much smaller in small discs (30-, 300- and 150-fold, respectively). During growth, an increase in D_0 and k_{off} expands the gradient, whereas an increase of k_{on} has the opposite effect (see equation (1)). Together, these changes underlie the scaling of the gradient (Supplementary Information section 3.8, Extended Data Fig. 7a).

Although in late discs the recycling module contributes to 90% of λ^2 (Fig. 3b), in earlier discs, the contribution of the recycling module is only 44% and the rest corresponds mostly to the unbound module (51%; Fig. 3b). This correlates with a larger extracellular pool of molecules measured in earlier discs ($\rho = 0.43 \pm 0.02$), compared to later discs

($\rho = 0.13 \pm 0.01$; Fig. 2g). Furthermore, the iFRAP experiment showed a reduced recovery in the ROI in small discs (Fig. 4e–g), consistent with a reduced effect of the recycling module (Fig. 3b, Extended Data Fig. 5i).

The importance of the recycling module versus the unbound module for λ^2 can be determined by looking at the ratio of the corresponding two terms (Fig. 1e, f, Extended Data Fig. 7b). In this ratio, k_{off} is the only rate that is different between small and large discs (see also Supplementary Information section 3.6). The larger the k_{off} rate, the smaller the relative contribution of the unbound module. Owing to the increase in k_{off} from smaller to larger discs, the unbound module becomes negligible and the recycling module dominates, expanding the gradient as the disc grows. Our analysis below suggests that Pentagone mediates this shift.

Pentagone in scaling by recycling

The extracellular factor Pentagone has been shown to act in a long-range manner and be involved in the scaling of Dpp signalling readouts in imaginal discs^{2,5,7,8} (Extended Data Fig. 7c–e, Supplementary Information section 4.1). Consistently, the scaling of the GFP–Dpp ligand itself is impaired in *pentagone* mutants (Fig. 2a, Extended Data Fig. 7f). We sought to address the question of which Dpp transport step is modulated by Pentagone during scaling.

For discs of similar sizes, Fig. 3c, d shows different clusters of parameter values in large control and *pentagone* mutant conditions (*pent²*, $l = 130 \pm 5 \mu\text{m}$). These clusters are very far from each other. The *pent²* cluster is closer to the cluster for small control discs (Fig. 3c, d). Indeed, in *pent²*, as in small discs, D_0 , k_{on} and k_{off} are all reduced in comparison to the large disc controls. However, k_{off} is sixfold smaller in *pent²* than in small discs. As a result, in *pentagone* mutants, the unbound module contributes to 97% of λ^2 and the other transport modules, including the recycling module, have a negligible contribution (Fig. 3b): *pentagone* mutants operate in an ExD-type of regime. Similar results were obtained in *pent²* small discs ($l = 85 \mu\text{m}$; Extended Data Fig. 7g–i). This ExD-type regime in *pent²* differs from the ExD scenario that has been proposed in the literature (Extended Data Fig. 1k, Supplementary Information section 4.2), in which the proposed extracellular diffusivity is much larger³⁴.

The three conditions studied (*pent²*, small and large discs) each show a different Dpp transport regime. The ratio of recycling versus unbound modules in these three conditions is represented as isolines in Fig. 3d. Indeed, the *pent²*, small and large disc clusters are separated by isolines that define three different regimes: dominating unbound module (*pent²*); combined unbound and recycling module (small discs); and dominating recycling module (large discs).

Therefore, Pentagone mediates scaling by engaging the recycling module. In *pentagone* mutants, the decay length remains short from small to large discs and this shorter decay length is caused by lower values of D_0 , k_{on} and k_{off} . In the wild type, as the tissue grows, Dpp gradient scaling is mediated by Pentagone-dependent changes in D_0 , k_{on} and k_{off} that progressively engage the recycling of internalized Dpp molecules in the process of gradient formation. The progressive changes in D_0 , k_{on} and k_{off} can be mediated by a progressive increase in Pentagone concentration during tissue growth (Extended Data Fig. 7j, k). Indeed, in the expansion–repression model for gradient scaling, Pentagone concentration increases as the tissue grows and the increasing concentration mediates the expansion of the Dpp gradient⁵.

Dally in scaling by recycling

Pentagone binds Dally, an HSPG associated by a glycosylphosphatidylinositol (GPI) anchor to the plasma membrane^{13,38}. It is well established that *dally* mutations affect the range of the Dpp gradient³⁹. Here, we show that scaling of Dpp gradients in *dally* mutant discs is perturbed: in discs of increasing size, the gradient remains short (Extended Data Fig. 8a, b). As in *pentagone* mutants, in *dally* mutants, D_0 , k_{on} and k_{off} are reduced and do not engage the recycling module (Extended Data Fig. 8c, d), which accounts for the scaling phenotype (see also Supplementary Information section 4.5.1).

In addition, Dally binds Dpp⁴⁰ and it can act on Dpp by facilitating its diffusion in the extracellular matrix milieu³⁹. This could explain how Pentagone and Dally influence D_0 . Furthermore, Dally is internalized^{33,41–45} and can therefore act as one of the internalization receptors that mediate Dpp endocytosis. We speculate that, if Dally does function as one of the receptors that internalize Dpp, then the k_{on} and k_{off} rates that are regulated by Pentagone could include the binding and unbinding rates of Dpp to Dally, although Pentagone may also regulate other unknown receptors in addition to Dally (for further discussion on how Pentagone and Dally could modulate D_0 , k_{on} and k_{off} , see Supplementary Information sections 4.5.2–4.5.4). Consistently, cleaving HSPGs from the membrane by phosphatidylinositol-phospholipase C (PI-PLC) and abolishing their function by downregulating the expression of Sulfateless by RNAi markedly affected the internalization of GFP–Dpp and the range of the gradient (Extended Data Fig. 8e–i; see also ref. ⁴⁶ and Extended Data Fig. 8j–m for controls).

Our work suggests that Pentagone mediates scaling by modifying the binding and unbinding properties of Dpp, both to its internalization receptor (possibly Dally) and to the extracellular matrix. Pentagone modulates these extracellular parameters, which in turn control the importance of recycling for transport. During scaling, Pentagone serves as a clutch to engage the recycling module as the tissue grows to drive the system between transport regimes.

Online content

Any methods, additional references, Nature Research reporting summaries, source data, extended data, supplementary information, acknowledgements, peer review information; details of author contributions and competing interests; and statements of data and code availability are available at <https://doi.org/10.1038/s41586-021-04346-w>.

- Rogers, K. W. & Schier, A. F. Morphogen gradients: from generation to interpretation. *Annu. Rev. Cell Dev. Biol.* **27**, 377–407 (2011).
- Wartlick, O., Julicher, F. & Gonzalez-Gaitan, M. Growth control by a moving morphogen gradient during *Drosophila* eye development. *Development* **141**, 1884–1893 (2014).
- Wartlick, O. et al. Dynamics of Dpp signaling and proliferation control. *Science* **331**, 1154–1159 (2011).
- Averbukh, I., Ben-Zvi, D., Mishra, S. & Barkai, N. Scaling morphogen gradients during tissue growth by a cell division rule. *Development* **141**, 2150–2156 (2014).
- Ben-Zvi, D., Pyrowolakis, G., Barkai, N. & Shilo, B. Z. Expansion-repression mechanism for scaling the Dpp activation gradient in *Drosophila* wing imaginal discs. *Curr. Biol.* **21**, 1391–1396 (2011).
- Fried, P. & Iber, D. Dynamic scaling of morphogen gradients on growing domains. *Nat. Commun.* **5**, 5077 (2014).
- Hamaratoglu, F., de Lachapelle, A. M., Pyrowolakis, G., Bergmann, S. & Affolter, M. Dpp signaling activity requires Pentagone to scale with tissue size in the growing *Drosophila* wing imaginal disc. *PLoS Biol.* **9**, e1001182 (2011).
- Zhu, Y., Qiu, Y., Chen, W., Nie, Q. & Lander, A. D. Scaling a Dpp morphogen gradient through feedback control of receptors and co-receptors. *Dev. Cell* **53**, 724–739 (2020).
- Inomata, H. Scaling of pattern formations and morphogen gradients. *Dev. Growth Differ.* **59**, 41–51 (2017).
- Romanova-Michaelides, M., Aguilar-Hidalgo, D., Julicher, F. & Gonzalez-Gaitan, M. The wing and the eye: a parsimonious theory for scaling and growth control? *Wiley Interdiscip. Rev. Dev. Biol.* **4**, 591–608 (2015).
- Entchev, E. V., Schwabedissen, A. & Gonzalez-Gaitan, M. Gradient formation of the TGF- β homolog Dpp. *Cell* **103**, 981–991 (2000).
- Kicheva, A. et al. Kinetics of morphogen gradient formation. *Science* **315**, 521–525 (2007).
- Stapornwongkul, K. S., de Gennes, M., Cocconi, L., Salbreux, G. & Vincent, J. P. Patterning and growth control in vivo by an engineered GFP gradient. *Science* **370**, 321–327 (2020).
- Akiyama, T. & Gibson, M. C. Decapentaplegic and growth control in the developing *Drosophila* wing. *Nature* **527**, 375–378 (2015).
- Matsuda, S. et al. Asymmetric requirement of Dpp/BMP morphogen dispersal in the *Drosophila* wing disc. *Nat. Commun.* **12**, 6435 (2021).
- Posakony, L. G., Raftery, L. A. & Gelbart, W. M. Wing formation in *Drosophila melanogaster* requires decapentaplegic gene function along the anterior–posterior compartment boundary. *Mech. Dev.* **33**, 69–82 (1990).
- Aguirre-Tamaral, A. & Guerrero, I. Improving the understanding of cytoneme-mediated morphogen gradients by in silico modeling. *PLoS Comput. Biol.* **17**, e1009245 (2021).
- Rojas-Rios, P., Guerrero, I. & Gonzalez-Reyes, A. Cytoneme-mediated delivery of hedgehog regulates the expression of bone morphogenetic proteins to maintain germline stem cells in *Drosophila*. *PLoS Biol.* **10**, e1001298 (2012).

19. Roy, S., Huang, H., Liu, S. & Kornberg, T. B. Cytoneme-mediated contact-dependent transport of the *Drosophila* decapentaplegic signaling protein. *Science* **343**, 1244624 (2014).
20. Aguilar Hidalgo, D., Hadjivasilou, Z., Romanova-Michaelides, M., González-Gaitán, M. & Jülicher, F. Dynamic modes of morphogen transport. Preprint at <https://arxiv.org/abs/1909.13280> (2019).
21. Wolpert, M. K. A. L. Mechanisms for positional signalling by morphogen transport: a theoretical study. *J. Theor. Biol.* **191**, 103–114 (1998).
22. Harmansa, S., Hamaratoglu, F., Affolter, M. & Caussinus, E. Dpp spreading is required for medial but not for lateral wing disc growth. *Nature* **527**, 317–322 (2015).
23. Felder, S., LaVin, J., Ullrich, A. & Schlessinger, J. Kinetics of binding, endocytosis, and recycling of EGF receptor mutants. *J. Cell Biol.* **117**, 203–212 (1992).
24. Hatta, T. et al. Identification of the ligand-binding site of the BMP type IA receptor for BMP-4. *Biopolymers* **55**, 399–406 (2000).
25. Kirchhausen, T., Owen, D. & Harrison, S. C. Molecular structure, function, and dynamics of clathrin-mediated membrane traffic. *Cold Spring Harb. Perspect. Biol.* **6**, a016725 (2014).
26. Kural, C. et al. Dynamics of intracellular clathrin/AP1- and clathrin/AP3-containing carriers. *Cell Rep.* **2**, 1111–1119 (2012).
27. Mineur, P. et al. Newly identified biologically active and proteolysis-resistant VEGF-A isoform VEGF111 is induced by genotoxic agents. *J. Cell Biol.* **179**, 1261–1273 (2007).
28. Sigismund, S. et al. Clathrin-mediated internalization is essential for sustained EGFR signaling but dispensable for degradation. *Dev. Cell* **15**, 209–219 (2008).
29. Wang, Y., Wang, X., Wohland, T. & Sampath, K. Extracellular interactions and ligand degradation shape the nodal morphogen gradient. *Elife* **5**, e13879 (2016).
30. Waters, C. M., Oberg, K. C., Carpenter, G. & Overholser, K. A. Rate constants for binding, dissociation, and internalization of EGF: effect of receptor occupancy and ligand concentration. *Biochemistry* **29**, 3563–3569 (1990).
31. Allendorph, G. P., Isaacs, M. J., Kawakami, Y., Izpisua Belmonte, J. C. & Choe, S. BMP-3 and BMP-6 structures illuminate the nature of binding specificity with receptors. *Biochemistry* **46**, 12238–12247 (2007).
32. Schwank, G. et al. Formation of the long range Dpp morphogen gradient. *PLoS Biol.* **9**, e1001111 (2011).
33. Hemalatha, A., Prabhakara, C. & Mayor, S. Endocytosis of Wingless via a dynamin-independent pathway is necessary for signaling in *Drosophila* wing discs. *Proc. Natl Acad. Sci. USA* **113**, E6993–E7002 (2016).
34. Zhou, S. et al. Free extracellular diffusion creates the Dpp morphogen gradient of the *Drosophila* wing disc. *Curr. Biol.* **22**, 668–675 (2012).
35. Khmelinskii, A. et al. Tandem fluorescent protein timers for in vivo analysis of protein dynamics. *Nat. Biotechnol.* **30**, 708–714 (2012).
36. Shcherbo, D. et al. Far-red fluorescent tags for protein imaging in living tissues. *Biochem. J.* **418**, 567–574 (2009).
37. Zerial, M. & McBride, H. Rab proteins as membrane organizers. *Nat. Rev. Mol. Cell Biol.* **2**, 107–117 (2001).
38. Vuilleumier, R. et al. Control of Dpp morphogen signalling by a secreted feedback regulator. *Nat. Cell Biol.* **12**, 611–617 (2010).
39. Fujise, M. et al. Dally regulates Dpp morphogen gradient formation in the *Drosophila* wing. *Development* **130**, 1515–1522 (2003).
40. Akiyama, T. et al. Dally regulates Dpp morphogen gradient formation by stabilizing Dpp on the cell surface. *Dev. Biol.* **313**, 408–419 (2008).
41. Guha, A., Sriram, V., Krishnan, K. S. & Mayor, S. Shibire mutations reveal distinct dynamin-independent and -dependent endocytic pathways in primary cultures of *Drosophila* hemocytes. *J. Cell Sci.* **116**, 3373–3386 (2003).
42. Gupta, G. D. et al. Analysis of endocytic pathways in *Drosophila* cells reveals a conserved role for GBF1 in internalization via GEECs. *PLoS ONE* **4**, e6768 (2009).
43. Mayor, S., Parton, R. G. & Donaldson, J. G. Clathrin-independent pathways of endocytosis. *Cold Spring Harb. Perspect. Biol.* **6**, a016758 (2014).
44. Sabharanjak, S., Sharma, P., Parton, R. G. & Mayor, S. GPI-anchored proteins are delivered to recycling endosomes via a distinct cdc42-regulated, clathrin-independent pinocytic pathway. *Dev. Cell* **2**, 411–423 (2002).
45. Norman, M., Vuilleumier, R., Springhorn, A., Gawlik, J. & Pyrowolakis, G. Pentagone internalises glypicans to fine-tune multiple signalling pathways. *Elife* **5**, e13301 (2016).
46. Yan, D. & Lin, X. Shaping morphogen gradients by proteoglycans. *Cold Spring Harb. Perspect. Biol.* **1**, a002493 (2009).

Publisher's note Springer Nature remains neutral with regard to jurisdictional claims in published maps and institutional affiliations.

© The Author(s), under exclusive licence to Springer Nature Limited 2021

Methods

Cloning

pUASTDpp Timer and GBP–Dendra2. Plasmid p744_p3E_mkate2sfGFP (a gift from E. Doná) was used as a template for the amplification of a fragment mkate2sfGFP with the following oligos:

mkate_pMt up TCCAGTGTGGTGAATTCTGCAGATATGGTGAGCG AGCTGATTAAG and sfGFP_pMt low AGACTCGAGCGGCCCGCCACTG TGCTAGATACCGGTGCTGCCCTTGTACAG. This 1.5-kb mkate2sfGFP fragment was used as a donor to swap GFP in pMT_Dpp-GFP using site-directed mutagenesis (Herculase II Fusion DNA Polymerase, Agilent Technologies, 3.5-min elongation). The resulting plasmid, pMT_Dpp-mkate2sfGFP, was used as a template to amplify the 3.265-bp Dpp-mkate2sfGFP fragment with the following oligos: FseI Dpp up ATTCGGCCGGCCCATGCGCGCATGGCTTACTCC and Ascl Dpp low CCATGGCGGCCCTATCGACGCCACAGCCACC. This fragment was cloned into pUAST FA blue between the Ascl/FseI restriction sites. The final plasmid (pUASTDpp Timer) (clone no. 8) was verified by sequencing. It was injected into *w¹¹¹⁸* embryos and screened for *w⁺* transformants (BestGene).

Plasmid pUAST4_dendra2 was used as template for the amplification of a fragment Dendra2 with the following oligos:

CCCAGGTTACCGTTAGCTCTGGCGGAGGAGGCTCGGGTGGCGGCGG CAGCATGAACACCCCGGGAATTA and AAGCTCGCCCTTGGCGGCC CTACTACCACACTGGCTGGGCA. The amplified DNA fragment was inserted at the C terminus of GBP in pET28b His Avitag PC TEV FA GBP using site-directed mutagenesis, as described above.

eGFP-Dpp^{CRISPR}. ChiRNA cloning. For the identification of the gRNAs, the flyCRISPR Target Finder⁴⁷ was used and the two guides (a) GGGCGG TGGAAGGGCGGC and (b) GTTGTAGTGGATGGCTGGTA designed. Two oligos for each guide (a) CTTCGGGCGGTGCAAGGGCGGC/AAACGCC GCCCTTGCCACCGCCC and (b) CTTCGTTGAGTGGATGGCTGGTA/AACTACCAGCCATCCACTCAAC were annealed and the DNA fragments were cloned in pU6-BbsI-chiRNA plasmid vector (Addgene 45946 (ref. 48)) using BbsI restriction site to produce pU6-Dpp-chiRNA and pU6-Dpp-chiRNAb.

Repair plasmid GFP-Dpp^{CRISPR} cloning and injections. For the cloning of the Dpp repair plasmid the pBS SK(+) was modified to add FseI and Ascl sites. The GFP was inserted in Dpp exon 6, between the furin sites RSIR and RNKR¹¹. An FseI/XhoI 1-kb homology left fragment, 5' of the insertion site of the GFP, was PCR-amplified using oligos GATCGGCCG CCAGATCCGAAAAGGTAGGCCG and CCATCTCGAGGCCGCCCTTGCC ACCGCCCTC. An EcoRI/Ascl 1-kb homology right fragment in the Dpp 3'-UTR was amplified with oligos GAGTGAATTCGATGGGAAATCGCG AGCGAG and GATCGGCCGCGCGCTGAGCTTACGCGTTAGGTC. An XhoI/EcoRI synthetic fragment of 1.7 kb containing the eGFP, the last part of exon 6 codon optimized to avoid recombination, a polyA and a fluorescent marker 3xP3:DsRed surrounded by loxP sites was ordered at Life Technologies. All of these fragments were sequentially cloned in the pBS SK(+) FseI/Ascl by restriction digestion.

Six hundred embryos *y[1]M{vas-Cas9.RFP-ZH-2A w[1118]}* (BDSC 55821) were injected with 500 ng μl^{-1} of Dpp repair donor plasmid 'site 1' and 125 ng μl^{-1} of pU6-Dpp-chiRNA. One hundred G0 adults were crossed to *y w* flies. One 3xP3:DsRed positive fly was identified (BestGene). Amplification and sequencing with either primers Dpp_Fd (TGGCTCTTGTGCAAGGTAC)/DsRed_Rv (GGAGCCGTACTGG AACTGGG) or DsRed_Fd (CTACAAGAAGCTGTCCCTCC)/Dpp_Rv (AGCAGGCATCCATAGGTCGC) confirmed the insertion.

The Pax3:DsRed cassette was removed using the Cre recombinase stock *yw; TM6B, Cre[w+]/MKRS, hsFlp[ry+]* (BDSC 1501), a gift from F. Karch.

UAS Pentagone::GFP. Pentagone::GFP MiMIC. The line was obtained by cassette exchange of the insertion MI02087 (*y[1] w[*]; Mi{y[+mDint2]=MIC}magu[MI02087]/SM6a*) from the MiMIC RMCE collection¹¹ (Gene disruption project). This line was crossed with the

M{vas-int.Dm}ZH-2a line producing phiC31 recombinase. Embryos were injected with plasmid no.1314 (DGRC) (pBS-KS-attB1-2-PT-SA-SD-2-EGFP-FIAsH-StrepII-TEV-3x-Flag) and balanced. The loss of *y* was used for the screening (BestGene). Orientation was checked using the following primers:

Orientation-MiL-F (GCGTAAGCTACCTTAATCTCAAGAAGAG) and EGFPdo-Seq-R (GTGGCTGTGAAGTTGTAATC).

UAS Pentagone::GFP. RNA and cDNA from the Pentagone::GFP MiMIC were prepared. Pent::GFP was amplified using the cDNA and cloned into pUAST into the FseI/NotI sites. The right clone was injected by BestGene.

UAS-sGFP^{Dpp}. Similarly to UAS-sGFP described previously¹¹, UAS-sGFP^{Dpp} was generated from UAS-GFP-Dpp by introducing a stop codon at the GFP C terminus (see scheme in Extended Data Fig. 2d).

Visualizing Dpp

In this report, we have used two systems expressing eGFP-Dpp described below: we generated eGFP-Dpp^{CRISPR} using the CRISPR-Cas9 technique and eGFP-Dpp^{LOP} reported previously²².

eGFP-Dpp^{CRISPR}/+. We have tagged endogenous Dpp by GFP fluorophore using the CRISPR-Cas9 technique (see 'eGFP-Dpp^{CRISPR}' subsection above). eGFP-Dpp^{CRISPR} flies have been used to evaluate the levels of expression of eGFP-Dpp using LexA/LOP and Gal4/UAS overexpression systems as compared to the endogenous levels of Dpp (Extended Data Fig. 3a). Note that eGFP-Dpp^{CRISPR} is not viable in homozygosis. This could be due to the linker flanking eGFP. The levels of eGFP-Dpp expression in heterozygosis are insufficient to detect the necessary amount of eGFP-Dpp fluorescence for the FRAP experiment, necessary for parameterization. This reagent was therefore not used for the full parameterization in this report. Nevertheless, we confirmed that the behaviour of eGFP-Dpp^{CRISPR} at endogenous levels is similar to the behaviour of eGFP-Dpp^{LOP} by performing the nanobody uptake assay and photoconversion assay in this condition (Extended Data Fig. 8l, m), which show similar results.

To confirm scaling of the eGFP-Dpp^{CRISPR} gradient, we measured the decay length of the spatial profile of internalized molecules, visualized by Alexa555 following GBP-Alexa555 internalization. We incubated live eGFP-Dpp^{CRISPR}-expressing discs in GBP-Alexa555 solution (0.04 μM in Clone 8 medium) for 45 min at 25 °C (see Supplementary Information section 2.2.2). Discs were then washed (3 times 15 min in Clone 8), fixed and mounted (see 'Mounting of fixed samples and immunostaining' subsection below). Alexa555 fluorescence in fixed samples was imaged (see 'Imaging of fixed samples' subsection below) and the fluorescence profile in space was fitted to an exponential function to estimate the decay length. We show for eGFP-Dpp^{CRISPR} that the internalized pool of nanobody forms a spatial gradient similar to eGFP-Dpp^{LOP} (Extended Data Fig. 3u, v). We can therefore use the decay length of the profile of internalized molecules as a proxy for the decay length of eGFP-Dpp^{CRISPR}. We show that the eGFP-Dpp^{CRISPR} gradient scales with a similar scaling factor to eGFP-Dpp^{LOP}: 0.17 \pm 0.06 versus 0.15 \pm 0.02, respectively (Extended Data Fig. 8j, k).

LOP-eGFP-Dpp/+; dppLG/+. eGFP-Dpp expression induced with a LexA driver in a *dpp* mutant background, as previously reported²², recapitulates the distribution and dynamics of endogenous Dpp, as concluded from the wild-type size and pattern of wings in this condition. Moreover, these eGFP-Dpp^{LOP}-expressing flies have previously been shown to reach adulthood. We evaluated the expression levels of eGFP-Dpp using a LexA/LOP overexpression system (Extended Data Fig. 3a) by performing a western blot analysis (see 'SDS-PAGE and western blot' subsection below). This system drives eGFP-Dpp expression at levels that are similar to those of endogenous Dpp, in contrast to overexpression by more than 10-fold with the previously used Gal4 system (1.1-fold overexpression with LexA/LOP versus 400-fold overexpression with Gal4/UAS, as quantified from the western blot (Extended Data Fig. 3a)).

Note that most experiments using eGFP-Dpp^{LOP} have been done in the presence of the endogenous gene and therefore they represent an overexpression condition. To test the effect of overexpression on dynamics of Dpp transport and the formation of the gradient, we performed nanobody uptake and FRAP assays on eGFP-Dpp^{LOP} in a condition in which we overexpress untagged Dpp under the control of *dppGal4* (Extended Data Fig. 3b–d). We observe no difference in the nanobody uptake and the FRAP recovery curves in the context of Dpp overexpression as compared to our experiments without overexpressing untagged Dpp.

Generation of *brk tkv* double-mutant clones

We have generated *brk tkv* double-mutant clones in the background of GFP-Dpp overexpression to check whether the internalization of GFP-Dpp was affected in the absence of *thickveins* (Fig. 4a, b). Clones were generated as previously described^{11,32} by heat-shocking second instar larvae 60 min at 37 °C. Discs of third instar larvae were dissected and subsequently incubated in a solution of GBP–Alexa555 (0.08 µM in Clone 8 medium) for 45 min, washed with ice-cold Clone 8 (2 washes of 15 min overall) and PBS (1 wash, 5 min) and fixed with 4% paraformaldehyde as described below. We have confirmed the absence of functional Tkv protein in *brk tkv* double mutant clones, with a P-Mad immunostaining: in the absence of Tkv, Mad is not phosphorylated (data not shown).

Immunoprecipitation

The procedure has been previously described⁴⁹. Imaginal discs of 100 third instar larvae were dissected and squashed into 500 µl of lysis buffer: 50 mM Tris; 150 mM NaCl; 50 mM sucrose; 5 mM EDTA; 5 mM ATP; 1 mM DTT; 0.3% Triton X-100; pH 7.5 and protease inhibitors (Complete mini tablets, Roche 05892791001). The extract was then incubated for 40 min at 4 °C on a rotating wheel, and cellular debris was cleared by centrifugation (16,000g, 10 min at 4 °C). Twenty-five microlitres of GFP-Trap beads slurry (Chromotek 090703001A) were equilibrated with Triton-free lysis buffer and incubated with the cleared extract. Immunoprecipitation was performed during 2 h at 4 °C with mild agitation. Beads were then washed three times with lysis buffer and finally resuspended in 35 µl Laemmli sample buffer. Samples were further processed for SDS–PAGE and western blot.

SDS–PAGE and western blot

Protein extracts (10 µl; cleared extracts or immunoprecipitates) were loaded on Nupage Bis Tris 4–12% gradient gels (Life Technologies). The gels were transferred to nitrocellulose membranes using iBLOT (Life Technologies). After the transfer, the membrane was rehydrated in distilled water and blocked during 30 min in PBT (PBS, 0.1% Tween-20, pH 7.5) with 5% non-fat dried milk. Primary antibodies, anti-GFP antibodies from mouse (Santa Cruz sc-9996), were diluted at 1 µg ml⁻¹ in blocking solution, and incubated overnight at 4 °C. The membrane was then washed 3 × 5 min in PBT, HRP-coupled secondary antibodies (Jackson ImmunoResearch 1:10,000 dilution) were diluted in blocking solution and incubated during 1 h at room temperature. The Benchmark Prestained Protein Ladder (Thermo Fisher Scientific 10748-010) was used to monitor protein sizes. Finally, western blots were revealed using Western Bright Quantum (Advantia) Chemiluminescent Substrate (Thermo Fisher Scientific 34080) and a Vilber Lourmat Fusion imager. See Extended Data Fig. 3a.

GBP and GBP–Dendra2 protein purification

His–GBP or His–GBP–Dendra2 have been purified as described previously⁴⁹. The plasmid pET28b His Avitag PC TEV FA GBP or GBP–dendra2 was transformed into Rosetta (DE3) competent cells (Sigma 70954). A 50-ml preculture was made in TB Kan (Terrific broth, kanamycin 30 µg ml⁻¹). The preculture was diluted 50-fold into 2 l TB Kan and grown at 37 °C to an optical density of 0.8 at 600 nm. It was then induced overnight at 22 °C with IPTG (Sigma I6558) at a final concentration of 0.5 mM.

Bacteria were pelleted, washed once with PBS and frozen at –20 °C. The pellet was thawed in 100 ml of cold lysis buffer (TBS, 1% Triton X-100, 10 mM MgCl₂, 5% glycerol, 4 mM imidazole, protease inhibitors (Roche cComplete EDTA-free Protease Inhibitor Cocktail COEDTAF-RO)). The suspension was sonicated 6 times 30 s (Branson Ultrasonics: output CTR: 7, duty cycle 60) on ice-water and pelleted in a Beckman JA25.5 rotor for 30 min at 14,000 rpm at 4 °C. The supernatant was incubated for 2 h at 4 °C with 2 ml of Talon Metal affinity Resin (Takara Clontech 635653) pre-equilibrated in lysis buffer. The slurry was then loaded on a column and washed with 50 ml of lysis buffer and then 100 ml of [20 mM HEPES, 150 mM KCl, 5% glycerol, 4 mM imidazole pH 7.7]. The protein was eluted in elution buffer [20 mM HEPES, 150 mM KCl, 5% glycerol, 300 mM imidazole pH 7.7] in 1-ml fractions and dialysed against [20 mM HEPES, 150 mM KCl, 5% glycerol pH 7.7] (or PBS for the labelling). It was then concentrated on Amicon Ultra-4 (Millipore UFC800324) down to 5 mg ml⁻¹ and ultracentrifuged on an Optima MAX-XP Benchtop Ultracentrifuge in a TLA100.1 rotor at 54,000 rpm (100,000g) for 10 min at 4 °C to get rid of the aggregates. Labelling of GBP by Alexa555 was performed according to the manufacturer's protocol using NHS-Alexa555 (A37571, Thermo Fisher Scientific).

Acid wash

To eliminate nanobody molecules labelling extracellular GFP-Dpp, we performed an acid wash. Live discs were washed with ice-cold Clone 8 with its pH dropped to 3 by HCl to unbind GFP-Dpp^{LOP} from the nanobody in the extracellular space (2 washes of 5 s each). To eliminate all stripped membrane-bound proteins, discs were then washed with large volumes (1 ml) of ice-cold clone 8 at physiological pH 7.4 (3 washes of 15 min overall) (see Extended Data Fig. 1e–h).

The acid wash efficiently eliminates extracellular nanobody molecules (reduces the extracellular staining down to 9%, see Extended Data Fig. 1e–h) as observed by performing an extracellular staining with GBP–Alexa555 in eGFP-Dpp-expressing discs (4 °C, without permeabilization) and comparing the signal before and after acid wash in two parallel sets of samples. Conversely, the acid wash did not significantly affect the intracellular signal: it reduces the intracellular signal only by 2.3 ± 0.6% (Extended Data Fig. 1i). This was assessed in a live experiment, by comparing endocytosed GBP–Alexa555 (45 min internalization) before and after acid wash.

This procedure was used in the iFRAP (Fig. 4c–g, Extended Data Fig. 5g, h) and the photoconversion experiment (Fig. 1a–c, Extended Data Fig. 1a, b).

Dependence of nanobody and GFP binding on pH

The anterior tip of CyO-GFP larvae were dissected and 25 samples were lysed in 0.5% Triton X-100, 0.5% Nonidet P-40, 50 mM Tris, pH 7.5, 100 mM NaCl, 5 mM EDTA and protease inhibitors (complete mixture from Roche) and processed for GFP pull-down using anti-GFP nanobody covalently bound to agarose beads (GFP-trap, Chromotek 090703001A), for 2 h at 4 °C. Beads were washed 3 × in lysis buffer, resuspended in 300 µl lysis buffer and aliquoted into 6 equal volumes of bead–lysis buffer slurry. To test the efficiency of GFP binding to GFP-trap, the supernatant (lane 1 in the blot of Extended Data Fig. 1j, FT: flowthrough) and the beads (lane 2 in the blot of Extended Data Fig. 1j, PD: pull-down) of one volume of bead–lysis buffer slurry were separated through centrifugation and were resuspended in 4 × Laemmli buffer. For the rest of the volumes, the beads were collected through centrifugation and each sample was resuspended in 50 µl 100 mM glycine solution adjusted to different pH values (4.5–2.5), for 10 s. Supernatants were collected and stored on ice, whereas the beads were washed 3 × in lysis buffer and their volume was reduced to 50 µl. Subsequently, both supernatants (Extended Data Fig. 1j, lanes 8–12) and bead fractions (Extended Data Fig. 1j, lanes 3–7) were supplemented with 4 × Laemmli buffer, boiled for 10 min and subjected to immunoblotting analysis using anti-GFP antibodies (1/1,000 dilution, Roche 11 814 460 001).

Mounting of fixed samples and immunostaining

Larvae were dissected in PEM (80 mM Na-PIPES, 5 mM EGTA, 1 mM MgCl₂ × 6H₂O, pH 7.4) and fixed with 4% paraformaldehyde in PEM for 35 min. The subsequent staining procedure is described in another study¹¹. For P-Mad immunostaining, rabbit-anti-P-Mad (PS-1)⁵⁰ was used (dilution 1:200). To label the anterior–posterior source boundary, mouse-anti-Drosophila Patched (deposited to the Developmental Studies Hybridoma Bank (DSHB) by I. Guerrero; DSHB Hybridoma Product Drosophila Ptc (Apa 1)) was used (dilution 1:50). To label the filamentous actin and therefore visualize the apical cortex of the cell membrane, F-actin phalloidin staining was performed. For this, fixed and permeabilized discs¹¹ were incubated in a solution containing Alexa Fluor 647 Phalloidin (dilution 1:100, Thermo Fisher Scientific, stock solution in methanol) in PEMT (PEM containing 0.1% Triton X-100) for 2 h at room temperature. Fixed discs were mounted using Vectashield.

PI-PLC treatment

PI-PLC treatment was used to abolish the function of *Drosophila* HSPGs Dally and Dally-like (Dlp)⁵¹ by releasing GPI-linked proteins away from their GPI anchor at the plasma membrane through incubation of live discs in a solution of Clone 8 medium containing 10 U ml⁻¹ of PI-PLC enzyme (Molecular Probes) as previously described⁵². After the incubation at 25 °C for longer than 1 h, HSPGs were entirely removed from the plasma membrane⁵².

Imaging of fixed samples

For eGFP-Dpp^{LOP} and GBP-Alexa555 imaging conditions, to ensure that fluorescence intensity accurately reflects the amounts of the fluorescent protein or dye, we routinely used a stepwise bleaching assay (not shown) as previously described³. This controls whether the fluorescence signal is proportional (linear relationship) to the concentration of molecules.

Mounting in a fibrinogen clot and live imaging

For experiments with live discs (nanobody uptake, FRAP and iFRAP), discs expressing eGFP-Dpp^{LOP} were mounted on a fluorodish (WPI, Fluorodish FD35-100) in Clone 8 medium using a clot of fibrinogen (341573, Calbiochem) and thrombin (27084601, 500 units per ml, GE Healthcare)⁵³ to attach the discs to the bottom of the dish. This procedure keeps the tissue healthy, as can be judged from active division of cells in the disc for up to 20 h (data not shown). Active cell division in the disc was used as a quality control for those experiments used for quantification in the nanobody uptake assay and the FRAP experiment.

Clone 8 medium was prepared by supplementing Shield and Sang M3 insect medium (S3652, Sigma) with 2% foetal bovine serum (FBS 10270-098, Invitrogen), 2.5% fly extract and 12.5 units of insulin (I1882, Sigma) per 100 ml⁵⁴.

Binning of data

Data in Fig. 2a, Extended Data Figs. 7c, f, k, 8a, b, j are represented as binned points in the plots. The coordinates of each bin correspond to the averages of the data values within the bin in both the x and the y axes. Standard errors around these averages in the x and y axes are also represented. As a consequence of this, the binned values are not equally spaced along the x axis. MATLAB code corresponding to the binning of control and *pent* mutant data in Fig. 2a is available upon request.

Data analysis

Image analysis was performed using ImageJ (v.2.0.0-rc-69/1.52p). Spatial gradient analysis was performed using MATLAB R2019b (9.7.0.1216025). Simulated data and nanobody recovery experimental data were analysed using Wolfram Mathematica 12.1.1.0. Excel v.16.36 and Prism 9 v.9.3.0 were also used.

Reproducibility

All micrographs (Figs. 1a, b, 2b, c, 4a–f, h–n, Extended Data Figs. 1a, b, e–j, 2a, e, g, r, 3a, b, f, o, q, s, u, 4a, g, 5g, h, 6a, c, h, k, 8h, i) were representative from a set of at least 3 independent experimental rounds and were in all cases reproducible. The same is true for the rest of the data in this report.

Randomization

Flies of the same genetic background were kept separate and each experiment was carried out on discs obtained from randomly chosen fly larvae of the appropriate genetic background and developmental stage. Our study does not explore the impact of different treatments on subjects, nor did it require sampling individuals that belong to different groups from large populations. Thus, randomization is not strictly relevant to our analysis.

Blinding

Our analysis did not involve quantifying the impact of treatments on different groups, so blinding was not necessary. Quantification was performed using the same programming scripts for all samples. Furthermore, the quantifications in all experiments were performed at the absence of information on the genetic background or developmental stage of samples.

Laboratory animals used

All experiments have been performed on *Drosophila melanogaster*, on wing discs of larvae of ages specified in the figure legends and of random sex (males and females). The genotypes used are specified in Supplementary Tables 1 and 2.

Reporting summary

Further information on research design is available in the Nature Research Reporting Summary linked to this paper.

Data availability

Source data are provided with this paper. Datasets generated during the parameter estimation are available in GitHub (<https://github.com/zenah12/DppTrafficking-/blob/main/README.md>). Source data are provided with this paper.

Code availability

Source codes are available in GitHub (<https://github.com/zenah12/DppTrafficking-/blob/main/README.md>). MATLAB code corresponding to the binning of control and *pent* mutant data in Fig. 2a is available upon request.

47. Gratz, S. J. et al. Highly specific and efficient CRISPR/Cas9-catalyzed homology-directed repair in *Drosophila*. *Genetics* **196**, 961–971 (2014).
48. Gratz, S. J. et al. Genome engineering of *Drosophila* with the CRISPR RNA-guided Cas9 nuclease. *Genetics* **194**, 1029–1035 (2013).
49. Derivery, E. et al. Polarized endosome dynamics by spindle asymmetry during asymmetric cell division. *Nature* **528**, 280–285 (2015).
50. Tanimoto, H., Itoh, S., ten Dijke, P. & Tabata, T. Hedgehog creates a gradient of DPP activity in *Drosophila* wing imaginal discs. *Mol. Cell* **5**, 59–71 (2000).
51. Eugster, C., Panakova, D., Mahmoud, A. & Eaton, S. Lipoprotein–heparan sulfate interactions in the Hh pathway. *Dev. Cell* **13**, 57–71 (2007).
52. Marois, E., Mahmoud, A. & Eaton, S. The endocytic pathway and formation of the Wingless morphogen gradient. *Development* **133**, 307–317 (2006).
53. Loubery, S. & Gonzalez-Gaitan, M. Monitoring notch/delta endosomal trafficking and signaling in *Drosophila*. *Methods Enzymol.* **534**, 301–321 (2014).
54. Montagne, C. & Gonzalez-Gaitan, M. Sara endosomes and the asymmetric division of intestinal stem cells. *Development* **141**, 2014–2023 (2014).

Acknowledgements We thank R. Mateus and I. Castanon Ortega for their feedback on the manuscript; F. Karch for Cre recombinase; K. Basler for the stock to make *brk^{M68} tkv⁹* mutant clones; E. Doná for the p744_p3E_mkate2sfGFP plasmid; M. Affolter for the LexA inducible

eGFP::DPP; K. Kruse for discussions; E. Derivery for the purified sfGFP-mKate2; V. Rasul-Kareeva for various contributions; and the Bioimaging Center of University of Geneva for microscopy support. Z.H. was supported by an HFSP long-term fellowship; and M.G.-G. was supported by the DIP of the Canton of Geneva, SNSF, the SystemsX EpiPhysX grant, the ERC (Sara and Morphogen) and the NCCR Chemical Biology program.

Author contributions M.R.-M. performed most experiments and quantifications and performed data analysis. D.A.-H., Z.H. and F.J. developed the theory and performed data analysis. Z.H. and D.A.-H. performed numerical simulations. C.S. cloned and made fly stocks to express Dpp^{Timer} and UAS Pentagone::GFP, performed immunoprecipitations and purified the GBP. D.B. performed the photoconversion experiment, labelled the purified GBP with Alexa555, cloned and purified GBP-Dendra2 and developed the acid wash. M.D. made the

Dpp^{CRISPR} stock. M.R.-M. and M.G.-G. conceived and designed experiments. M.R.-M. and Z.H. prepared figures. M.R.-M., Z.H., F.J. and M.G.-G. prepared the manuscript.

Competing interests The authors declare no competing interests.

Additional information

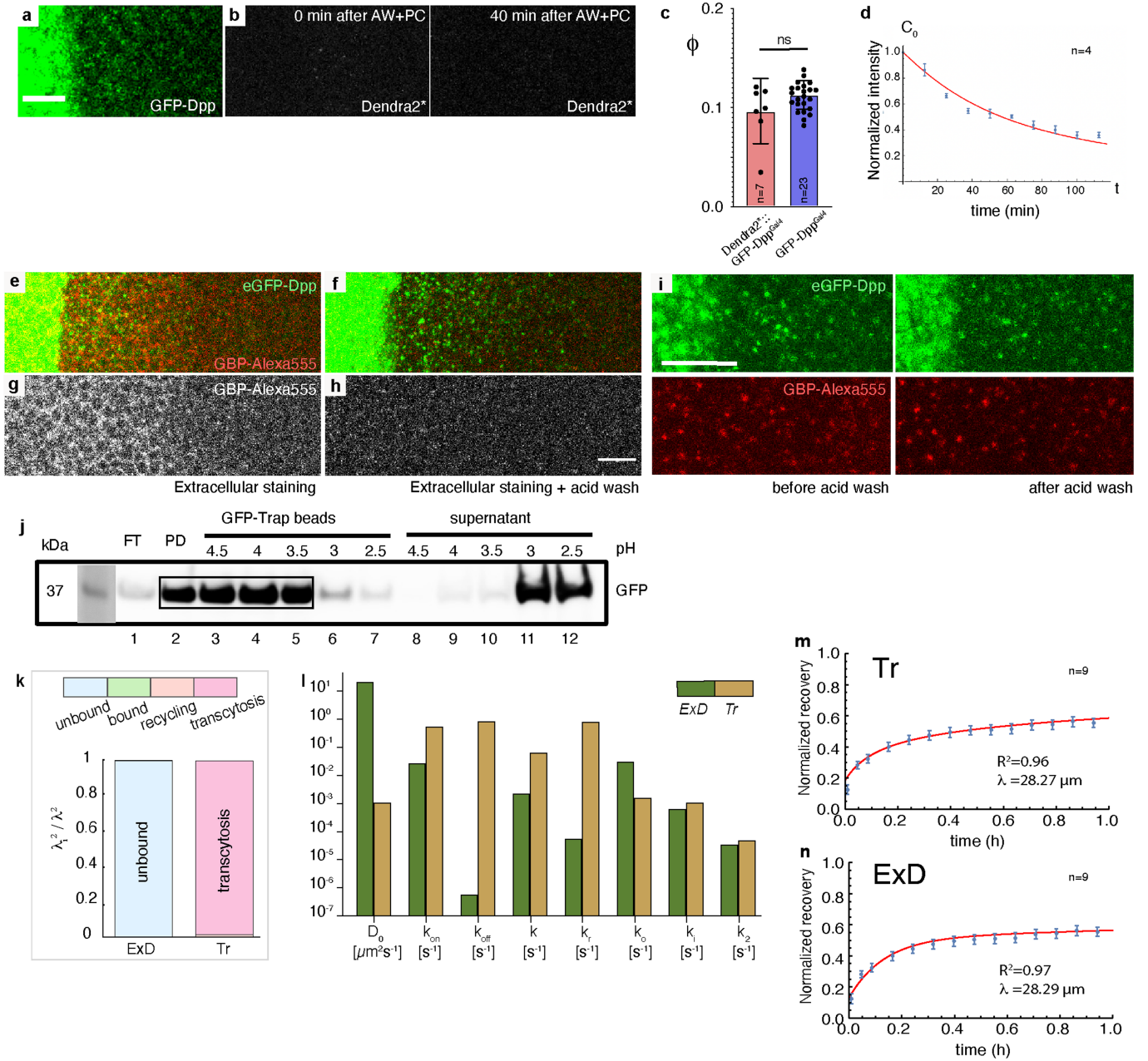
Supplementary information The online version contains supplementary material available at <https://doi.org/10.1038/s41586-021-04346-w>.

Correspondence and requests for materials should be addressed to Maria Romanova-Michaelides, Frank Jülicher or Marcos Gonzalez-Gaitan.

Peer review information *Nature* thanks Dagmar Iber, Timothy Saunders and the other, anonymous, reviewer(s) for their contribution to the peer review of this work. Peer reviewer reports are available.

Reprints and permissions information is available at <http://www.nature.com/reprints>.

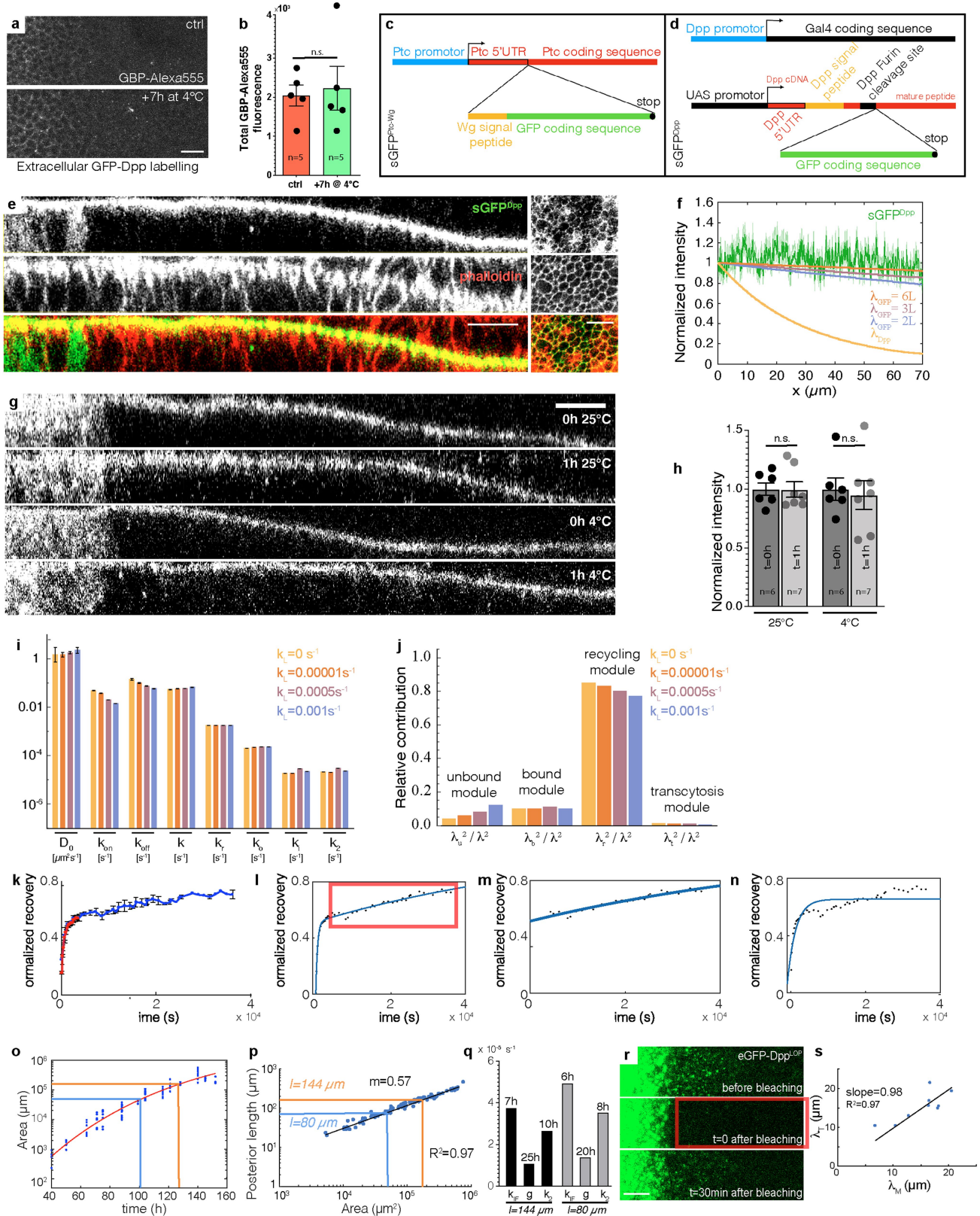
Article



Extended Data Fig. 1 | See next page for caption.

Extended Data Fig. 1 | Photoconversion assay controls and two extreme regimes of Dpp transport. a–d. Photoconversion assay. Test of efficiency of the acid wash in the photoconversion experiment using GBP-Dendra2: GFP-Dpp expressing discs have been incubated in GBP-Dendra2 for 50 min at 4 °C (the nanobody is only bound to the extracellular pool) and subsequently acid-washed to remove the label of the extracellular pool. Confocal image of eGFP-Dpp^{LOP} expressing disc (**a**) and corresponding images of Dendra2* (**b**) before photoconversion (left) and 40 min following photoconversion (right; see Materials and Methods). Note that no detectable Dendra2* signal is observed 40 min after the acid wash, indicating that the extracellular pool of nanobodies has been efficiently removed and that the potential extracellular leftover (below the detection limit) cannot lead to an observable recovery in intracellular compartments. **c.** Comparison between eGFP-Dpp^{Gal4} gradient profiles and gradient profiles formed by photoconverted Dendra2* propagated into the posterior compartment of the discs (photoconversion experiments as in Fig. 1a). Bar plot showing $\phi = \lambda/l$ of eGFP-Dpp^{Gal4} gradient profiles and photoconverted Dendra2* gradient profiles for large discs. Bars, standard deviations. Two-tailed two sample t-test, p-value = 0.2353. **d.** Fluorescence intensity of Dendra2* in a ROI of 6x35 μm at the source boundary in the photoconversion experiment in Fig. 1a. Measured Dendra2* fluorescence (blue dots) is plotted as a function of time after the photoconversion event. The red line represents the theoretical dynamics of Dendra2* fluorescence signal considering the parameterized values for large discs. n = 4 biologically independent samples. Data represented as mean values \pm s.e.m. **e–h.** Acid wash efficiently removes the extracellular pool. Confocal images of eGFP-Dpp^{LOP} gradient (green in **e, f**), and extracellular eGFP-Dpp^{LOP} pools monitored by means of an extracellular immunostaining (see Materials and Methods, Supplementary Information section 2.3.2) by using a GBP-Alexa555 nanobody against GFP (**g, h**; red in **e, f**) before (**e, g**) and after (**f, h**)

acid wash. Acid wash in these conditions largely reduces the extracellular staining down to 9% of the signal. Scale bar: 10 μm . **i.** Acid wash does not affect internalized GBP-Alexa555. Confocal images of eGFP-Dpp^{LOP} (top, green) and GBP-Alexa555 internalized for 40 min (bottom, red) before (left) and after acid wash (right). The GBP-Alexa555 signal decreases by $2.3 \pm 0.6\%$ after acid wash. **j.** Acid wash: effect of pH on GBP binding to GFP from larval extracts. Immunoblot of GFP which was bound to GFP-Trap beads (Chromotek, GFP-Trap beads, lanes 3-7) and GFP dissociated from GFP-Trap beads (supernatant, lanes 8-12) following treatment at different pH. FT, flowthrough (lane 1), PD, pulldown (lane 2). For gel source data, see Supplementary Fig. 1a. **k.** Stacked bar chart showing the relative contribution of the different modules to Dpp transport in the two theoretical extreme regimes of morphogen transport: extracellular diffusion (ExD²⁰) and transcytosis (Tr) regimes. The relative contribution of different modules is expressed as the ratio λ_i^2/λ^2 with the index i corresponding to each of the four modules ($i = u, b, r, t$). Note that the unbound module contributes almost exclusively to λ^2 in ExD and the transcytosis module, in Tr. **l.** Theoretical values of the 8 transport rates characteristic for ExD (rate values as in reference²⁰) and Tr regimes of morphogen transport. **m, n.** FRAP recovery with respect to the two extreme theoretical regimes. Red lines, calculated recovery curves in a FRAP experiment for a set of parameter values corresponding to the extreme Tr (**m**) and ExD¹⁷ regimes (**n**). Blue dots, average of the experimental recovery curves in discs of $l = 144 \mu\text{m}$ average posterior length. n = 9 biologically independent samples. Data represented as mean values \pm s.e.m. The coefficient of determination R^2 characterizes how well the calculated curves fit the experimental FRAP data. λ , decay length of the Dpp gradient profile calculated using equation (1) and the set of parameter values corresponding to Tr and ExD (see Supplementary Information section 4.2). Bars, s.e.m. Scale bar, 10 μm (**a, h, i**).

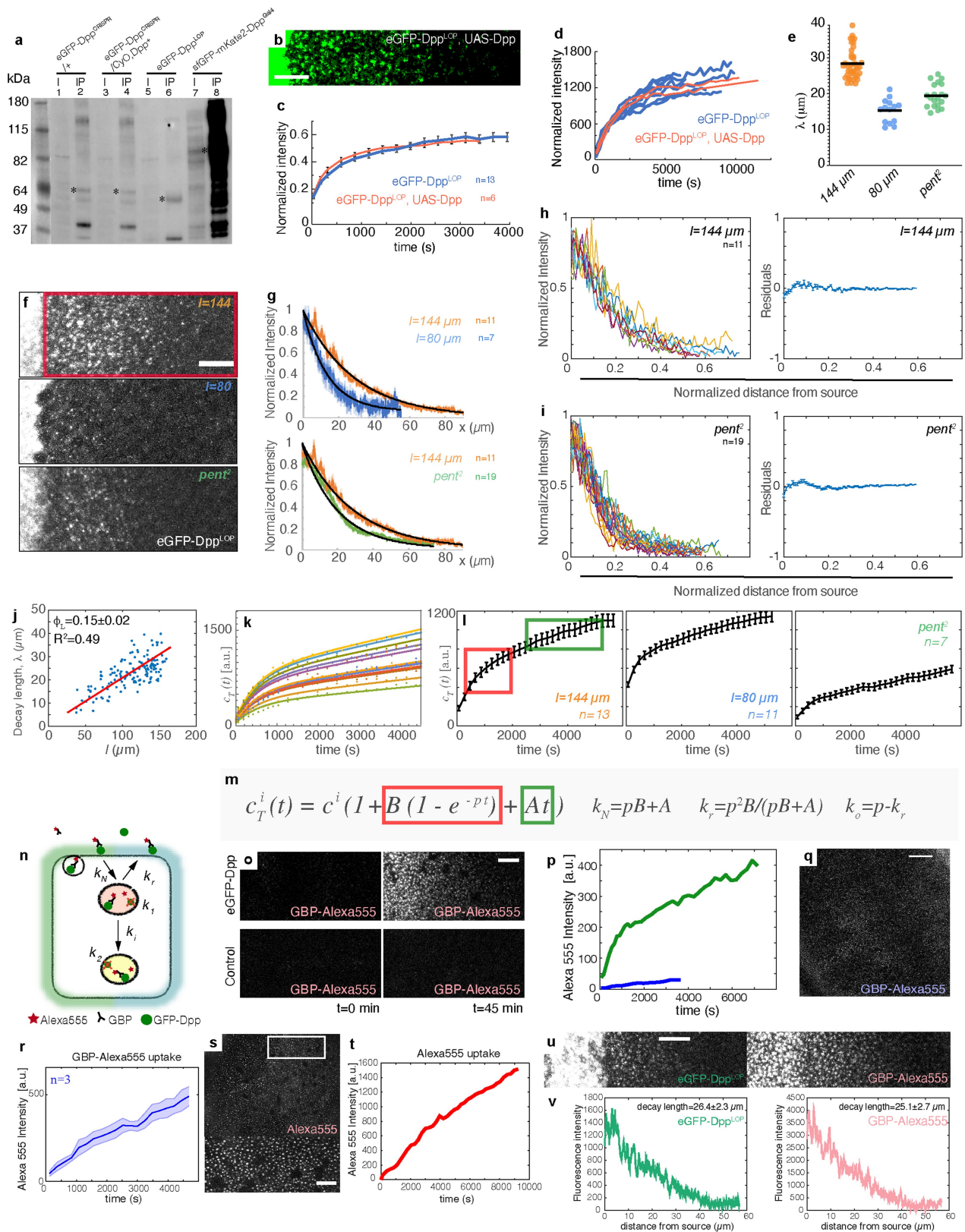


Extended Data Fig. 2 | See next page for caption.

Extended Data Fig. 2 | Analysis of Dpp leakage and effects of growth on Dpp gradient profile.

a, Confocal images of GBP-Alexa555 labelling extracellular GFP-Dpp in a control extracellular staining (top) and following a chase of living discs for 7 h at 4 °C. **b**, Total GBP-Alexa555 fluorescence in the conditions in **a**. Two-tailed two sample t-test, p-value = 0.7787. n, number of biologically independent samples. Bars, s.e.m. **c, d**, Schemes of sGFP^{Ptc-Wg}, see reference³¹ (**c**) and sGFP^{Dpp} constructs (**d**). Sizes of fragments represented in the scheme do not correspond to the nucleotide sequences. **e**, Confocal images of sGFP^{Dpp} (top), phalloidin staining (middle) and merge (bottom). Left panels, orthogonal views; right panels, xy plane. **f**, Normalized average spatial profile of sGFP^{Dpp} fluorescence (green) compared to the normalized profiles of gradients with decay lengths $\lambda = \lambda_{Dpp}$; $\lambda = 6L$; $\lambda = 3L$ and $\lambda = 2L$ with $\lambda_{Dpp} = 28.9 \mu\text{m}$ and $L = 144.6$, average posterior size of eGFP-Dpp^{LOP} third instar discs. **g**, Orthogonal views of confocal images of sGFP^{Dpp} fixed immediately after dissection (0 h) and following a chase of living discs for 1h at 25 °C and 4 °C. **h**, Total sGFP fluorescence in the conditions in **g**, normalized for each temperature to the value at t = 0 h. Two-tailed two sample t-test for unequal variances, p-values: 0.9792 (25 °C) and 0.7543 (4 °C). n, number of biologically independent samples. Bars, s.e.m. **i**, Effect of leakage on parameterization of Dpp transport rates. Average estimated parameters considering leakage rates $k_l = 0\text{s}^{-1}$; 0.00001s^{-1} ; 0.0005s^{-1} and 0.001s^{-1} . Simulations represent 3.7×10^6 randomly chosen parameter sets per condition. **j**, Stacked bar chart showing the relative contribution of the different modules to λ^2 (described in Fig. 1e,f) for conditions in **i**. n, sample size; bars, s.d. **k**, Long-term FRAP assay. Dynamics of fluorescence recovery in conventional FRAP for one hour (red) and long-term

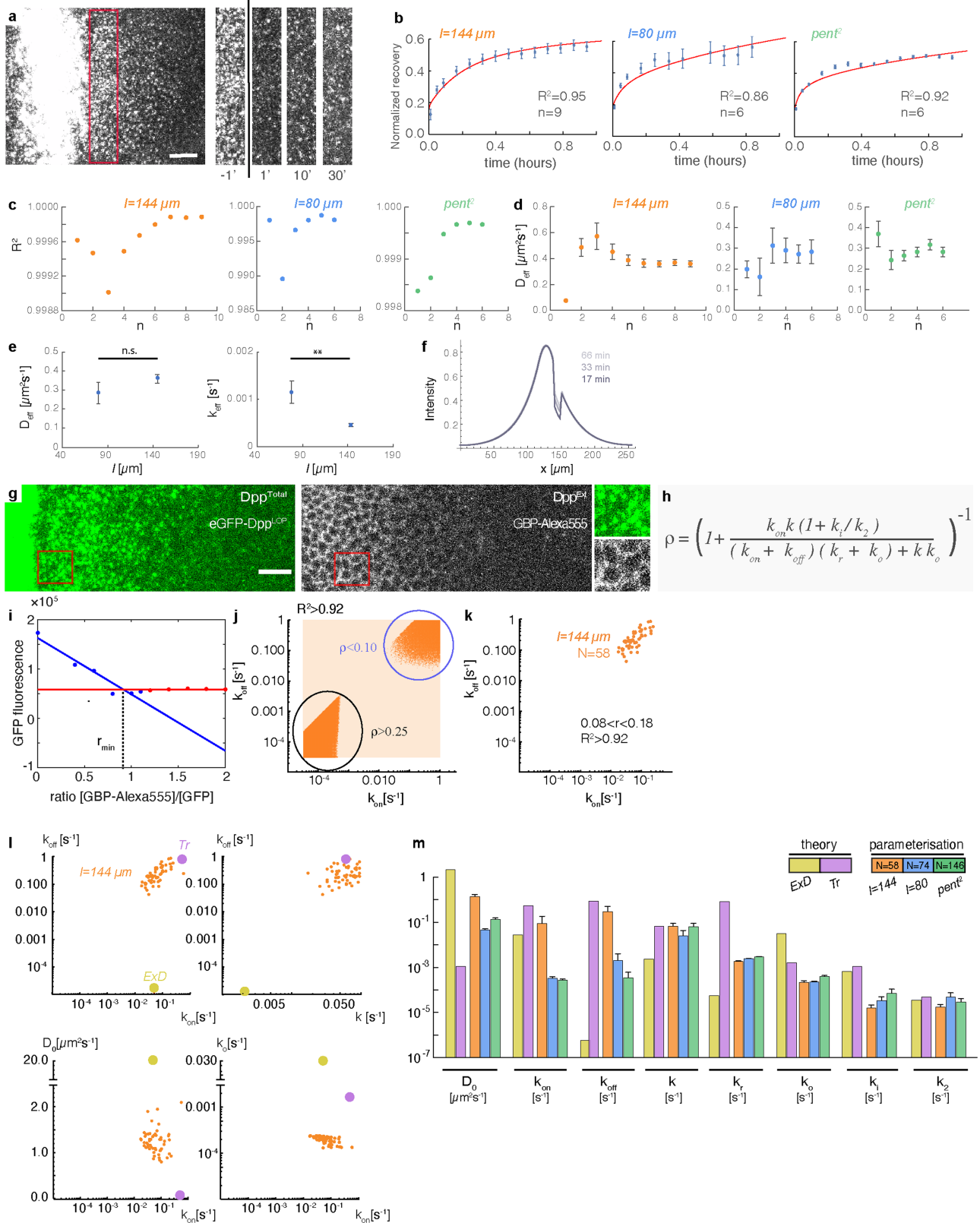
FRAP for ten hours (blue). Fluorescence recovery is normalized to the signal in the ROI before bleaching. Note that recovery of conventional FRAP overlays the dynamics of long-term FRAP at short time scales. Bars, s.e.m. **l, n**, Dynamics of long-term FRAP recovery and fit to double (**l**, blue line) and single exponential dynamics (**n**, blue line) to the dataset (both early and late). Box in **l**, late recovery (after 5,000 s) analysed in **m**. **m**, Dynamics of long-term FRAP recovery (late recovery) and single exponential fit (blue line) to the late slow dynamics. **o**, Wing disc area plotted as a function of disc age in staged larvae (hours after egg laying) and fit to an exponential growth in which growth rate decays exponentially over time (red line). See Supplementary Information section 2.9. Orange and blue lines correspond to area and age of discs of $l = 144 \mu\text{m}$ and $l = 80 \mu\text{m}$ posterior length, respectively, as determined by the plot in **p**. **p**, Posterior compartment length (l) as a function of wing disc area (A). Black line, power-law fit. Growth anisotropy $m = g_x/g_y = \frac{l/l'}{A/A'}$. Using m , the area of discs of $l = 144 \mu\text{m}$ and $l = 80 \mu\text{m}$ posterior length can be determined (orange and blue lines). **q**, Wing disc growth rate (g), relaxation rate of the slow dynamics (that of the immobile fraction, IF) in long-term FRAP (k_{IF}) and degradation rate of the immobile pool (k_2) estimated according to $k_2 = k_{IF} - g$. The timescales corresponding to these rates are indicated on top of bars. **r, s**, Measurement of the mobile pool decay length. **r**, Confocal images of eGFP-Dpp^{LOP} before (top) and at indicated times after bleaching (middle and bottom). **s**, Correlation between the decay length of the total pool of eGFP-Dpp at steady state (λ_T) measured before bleaching and the mobile pool decay length measured 30 min after bleaching (λ_M). Black line, linear regression. Note the slope close to 1, indicating that for discs of different sizes $\lambda_M \approx \lambda_T$. Scale bar, 10 μm (**a, e, g, r**).



Extended Data Fig. 3 | See next page for caption.

Extended Data Fig. 3 | Parameterization assay controls I: steady-state decay length and nanobody internalization. **a**, Immunoprecipitation of eGFP-Dpp under different expression systems. See Methods. Input (I) and immunoprecipitate (IP) from eGFP-Dpp^{CRISPR}/+ (lanes 1,2), eGFP-Dpp^{CRISPR}/CyO,Dpp* (lanes 3,4), dppLG/+; LOP-eGFP-Dpp/+ (lanes 5,6; eGFP-Dpp^{LOP}) and Dpp-Gal4/UAS-sfGFP-mKate2-Dpp larval head extracts (lanes 7,8). Mature GFP-Dpp fragment after Furin cleavages is marked by an asterisk. Note that GFP-Dpp amounts when expressed using LexA/LOP system are similar to the amounts of GFP-Dpp endogenously expressed (1.1 fold), whereas Gal4/UAS system expresses almost 400 fold more GFP-Dpp. For gel source data, see Supplementary Fig. 1b. **b**, Confocal image of eGFP-Dpp^{LOP} in the background of overexpression of Dpp by dppGal4. **c, d**, Dynamics of FRAP recovery (c) and nanobody uptake (d) in this condition (red lines) as compared to control (blue). Bars, s.e.m. **e**, Average decay length λ of the gradients considered in the three datasets, corresponding to the three conditions considered in this report: large discs (average posterior length $l = 144 \mu\text{m}$ in the dataset), small discs (average $l = 80 \mu\text{m}$) and in a *pent*² mutant disc (average $l = 130 \mu\text{m}$). Bars, standard error to the mean (s.e.m.). The average decay length for the average l corresponding to the three experimental conditions was estimated using the linear regression of eGFP-Dpp^{LOP} control (sample size $n = 157$ discs) and *pentagone* mutant ($n = 63$ discs) datasets (see Fig. 2a). **f**, Confocal images (maximum projections) of the eGFP-Dpp^{LOP} gradient (red box, region of interest (ROI) in the posterior compartment) in representative discs from the three conditions described in **b**. The source is to the left. **g**, Average spatial distribution of eGFP-Dpp^{LOP} in these datasets. Shaded areas, s.e.m. Black line, exponential fit. **h, i**, Left, normalized eGFP-Dpp^{LOP} profiles in large control discs (**h**; $l = 144 \mu\text{m}$) and *pent*² mutant disc (**i**; $l = 130 \mu\text{m}$); right, average residuals of the fits of these profiles to an exponential function. Bars, s.e.m. **j**, Scaling plot of eGFP-Dpp^{LOP}. Decay length (λ , from the exponential fit) of the eGFP-Dpp^{LOP} gradient versus l . Red line, linear regression. $\phi_l = \lambda/l$ determined from the linear regression. **k**, GBP-Alexa555 signal intensity as a function of time in 13 different discs. Lines, fits to the phenomenological $c_1^l(t)$ equation for the internalized signal intensity (left equation in **m**; red/green boxes as in **l**). **l**, Average dynamics of the GBP-Alexa555 fluorescence signal in the three conditions. Bars, s.e.m. **m**, Parameterization of k_N , k_o and k_r based on the dynamics of GBP-Alexa555 signal. Left, phenomenological $c_1^l(t)$ equation which captures the exponential (red box; see also **l**) and linear dynamics (green box) of the accumulation of the GBP-Alexa555 signal. Right, relationship between the phenomenological parameters A , B and p and k_N , k_o and k_r (see Supplementary Information section 2.2.1).

n, Scheme of the GBP-Alexa555 internalization assay. Rates and pools indicated, like in Fig. 1d. Note that the fluorophore (Alexa555; star) degrades on a time scale which is much longer than the duration of the experiment. **o**, Confocal images of internalized GBP-Alexa555 in a disc expressing eGFP-Dpp^{LOP} (top) and a control disc (bottom) at indicated timepoints of nanobody internalization using the same nanobody concentration as in Fig. 2b-f. Note that, under these conditions, fluid-phase internalization of the nanobody in the absence of eGFP-Dpp^{LOP} (bottom, control) is negligible compared to the internalization when bound to eGFP-Dpp^{LOP} (top, eGFP-Dpp). **p**, Dynamics of internalized GBP-Alexa555 in the disc expressing eGFP-Dpp^{LOP} (green curve) and a control disc (blue curve), in the same experimental conditions (e.g. same nanobody concentration) as in the nanobody uptake experiments in **o**. Note that, in these conditions, internalization of GBP-Alexa555 by fluid phase in the absence of GFP-Dpp is negligible. **q-r**, Dynamics of fluid-phase internalization of GBP-Alexa555. **q**, Confocal image of fluid-phase internalized GBP-Alexa555 (40 min of nanobody incubation) showing that, at high concentration of the nanobody, a signal can be detected at low levels which is homogenous in space (there is no gradient). Five-fold higher concentration of the nanobody than in **o** was used to reliably detect the signal of the fluid-phase internalized nanobody. **r**, Dynamics of fluid-phase internalized GBP-Alexa555 signal intensity, averaged over 3 independent experiments. Same concentration as in **p**. Shaded area, s.e.m. Note that the dynamics do not show the early exponential regime seen in the presence of eGFP-Dpp, indicating that the nanobody by itself is not significantly recycled. **s**, Top, confocal image of fluid-phase internalized Alexa555 (40 min of Alexa555 incubation). Also here, internalization of the fluorophore is homogeneous in space. Bottom, high magnification of the ROI area shown in the top. **t**, Dynamics of fluid-phase internalized Alexa555, showing a linear increase without saturation in the timescale of the experiment, which reflects a lack of degradation in the lysosome of the Alexa555 fluorophore. **u**, Confocal images of the eGFP-Dpp^{LOP} gradient (left) and internalized GBP-Alexa555 (right) after 45 min of incubation with the nanobody in a control large disc. The source is to the left. In contrast to the situation for fluid phase internalization (**p, r**), internalized eGFP-Dpp^{LOP} with GBP-Alexa555 is distributed as a gradient. **v**, Spatial profiles of the gradients in **u** in the posterior compartment. The decay length is determined by fitting the spatial profiles to an exponential function with an offset. The decay length is given with its confidence interval. n , number of biologically independent samples. Bars, s.e.m (**c, g, h, l, r**). Scale bars, 10 μm (**b, f, o, s, u**) and 50 μm , (**q**).



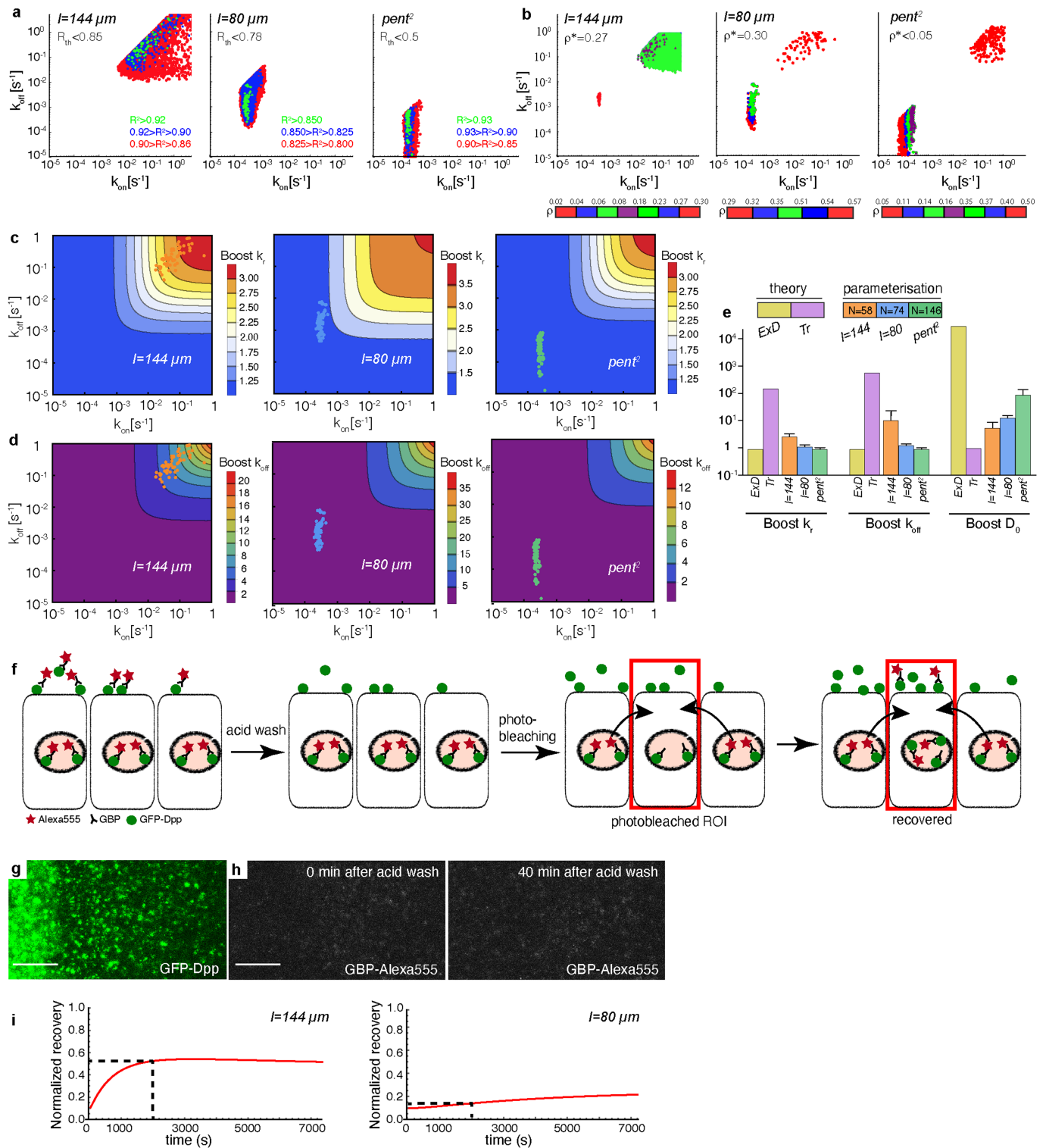
Extended Data Fig. 4 | See next page for caption.

Extended Data Fig. 4 | Parameterization assay controls II: FRAP, extracellular fraction determination and parameter estimation by ABC.

a, Left, confocal image of the eGFP-Dpp^{LOP} gradient in a FRAP experiment (source and posterior compartment). Red box, region to be photobleached. Right, eGFP-Dpp^{LOP} fluorescent signal in the red box region before photobleaching (-1 min) and at different times (as indicated below) after photobleaching. **b**, Average dynamics of fluorescence recovery in the bleached area in the three experimental conditions (discs of $l = 144 \mu\text{m}$ and $l = 80 \mu\text{m}$ posterior length and in a *pent*² mutant disc). Data represented as mean values. Bars, s.e.m. Lines, calculated recovery using the five-pool theoretical framework for a set of parameter values. The coefficient of determination R^2 characterizes how well the theoretical curves fit the FRAP data. **n**, sample size. **c, d**, Robustness analysis of the FRAP assay. The average FRAP trace was fitted by a single dynamic equation³. Dependence of the goodness of the fit (R^2) to this single dynamic equation (**c**) and the effective diffusivity (D_{eff}) estimated by this fit (**d**) on the number of individual recovery curves (n) considered for the average FRAP trace. The analysis was performed for the three experimental conditions of this report: large discs (average posterior length $l = 144 \mu\text{m}$ in the dataset; left), small discs (average $l = 80 \mu\text{m}$; centre) and *pent*² discs (right). Bars, confidence intervals (**d**). In **d** data are represented as D_{eff} estimated by fit for varying number of independent recovery curves, n . Bars, confidence intervals of fit. **e**, Effective diffusivity (D_{eff} , left) and effective degradation rate (k_{eff} , right) plotted against the average posterior length of discs within two datasets: small (average $l = 80 \mu\text{m}$) and large (average $l = 144 \mu\text{m}$). The average FRAP recovery curve was fitted by a single dynamic equation³ to determine D_{eff} and k_{eff} . Note, that as discs grow, D_{eff} does not change significantly, whereas k_{eff} decreases significantly, as previously reported²³. Data is represented as D_{eff} and k_{eff} estimated by fit. Bars, confidence intervals of fit. **n**, number of biologically independent samples. One-tailed two sample t-test with unequal variances; p-values: 0.1765 (D_{eff} , left) and 0.0038 (k_{eff} , right). **f**, Simulated intensity profile of eGFP-Dpp^{LOP} at indicated times after photobleaching in the ROI in the posterior compartment (experiment as in **a**). x , distance from the edge of the anterior compartment. Parameter values used in the simulations are those of our parameterization for $l = 144 \mu\text{m}$. **g**, Confocal images of the eGFP-Dpp^{LOP} gradient (left; total pool), and the extracellular eGFP-Dpp^{LOP} pools monitored by means of an extracellular

immunostaining (see Supplementary Information section 2.3) by using a GBP-Alexa555 nanobody against GFP (right; extracellular pool). Higher magnification of the fluorescent signal of the area boxed in the images are shown to the right. **h**, Expression of the extracellular fraction (ρ) as function of Dpp transport rates. **i**, Equimolarity of the GBP-Alexa555 and eGFP solutions used for calibration of the Alexa555 versus GFP fluorescent signal (see Methods, Supplementary Information section 2.3.2; relevant to the extracellular fraction determination assay). The concentrations of GBP-Alexa555 and eGFP was first roughly determined by means of a BCA assay (Supplementary Information section 2.3.2). Plot of GFP fluorescence intensity as a function of the ratio of GBP-Alexa555 and GFP concentrations (determined by BCA) in the solutions. The relative concentration of GFP and GBP-Alexa555 can be determined from the relative concentration at which the minimum value (r_{min}) of GFP fluorescence has been reached. Note that $r_{\text{min}} \approx 1$ confirms that the BCA estimation was already accurate. **j**, Parameter value sets determined by the parameterization procedure (see Supplementary Information section 2.5.2) are represented in the $(k_{\text{on}}, k_{\text{off}})$ plane. Light orange area represents the full space of 3×10^7 parameter value sets considered ($l = 144 \mu\text{m}$ dataset). Dark orange dots represent sets of parameter values within those which satisfy the constraints given by the steady-state decay length, the long-term FRAP assay, the nanobody internalization and the FRAP assay. Calculated FRAP recovery curves using these sets of values fit the experimental FRAP data with $R^2 > 0.92$. Note that the solutions are separated into two clusters (clouds): the upper cloud, with higher $k_{\text{on}}, k_{\text{off}}$, is characterized by a low extracellular fraction $\rho < 0.10$ and a lower cloud, by a high $\rho < 0.25$. **k**, Selected sets of parameter values from **j** for which the calculated extracellular fraction is within the experimentally determined range of ρ values ($0.08 < \rho < 0.18$). **l**, Sets of parameter values which satisfy all the constraints given by our assays (see Supplementary Information section 2.5.2), represented in $(k_{\text{off}}, k_{\text{on}})$, (k_{off}, k) , (D_0, k_{on}) and (k_0, k_{on}) planes. The parameter values corresponding to the two extreme theoretical cases discussed in Supplementary Information section 4.2 (Extracellular diffusion regime, ExD, yellow and Transcytosis regime, Tr, purple) are represented by circles for comparison. **m**, Average estimated parameters in the three experimental conditions compared to the theoretical values of parameters in ExD and Tr. Bars, s.d. N , number of parameterized sets of values. Scale bars: $10 \mu\text{m}$ (**a, g**).

Article



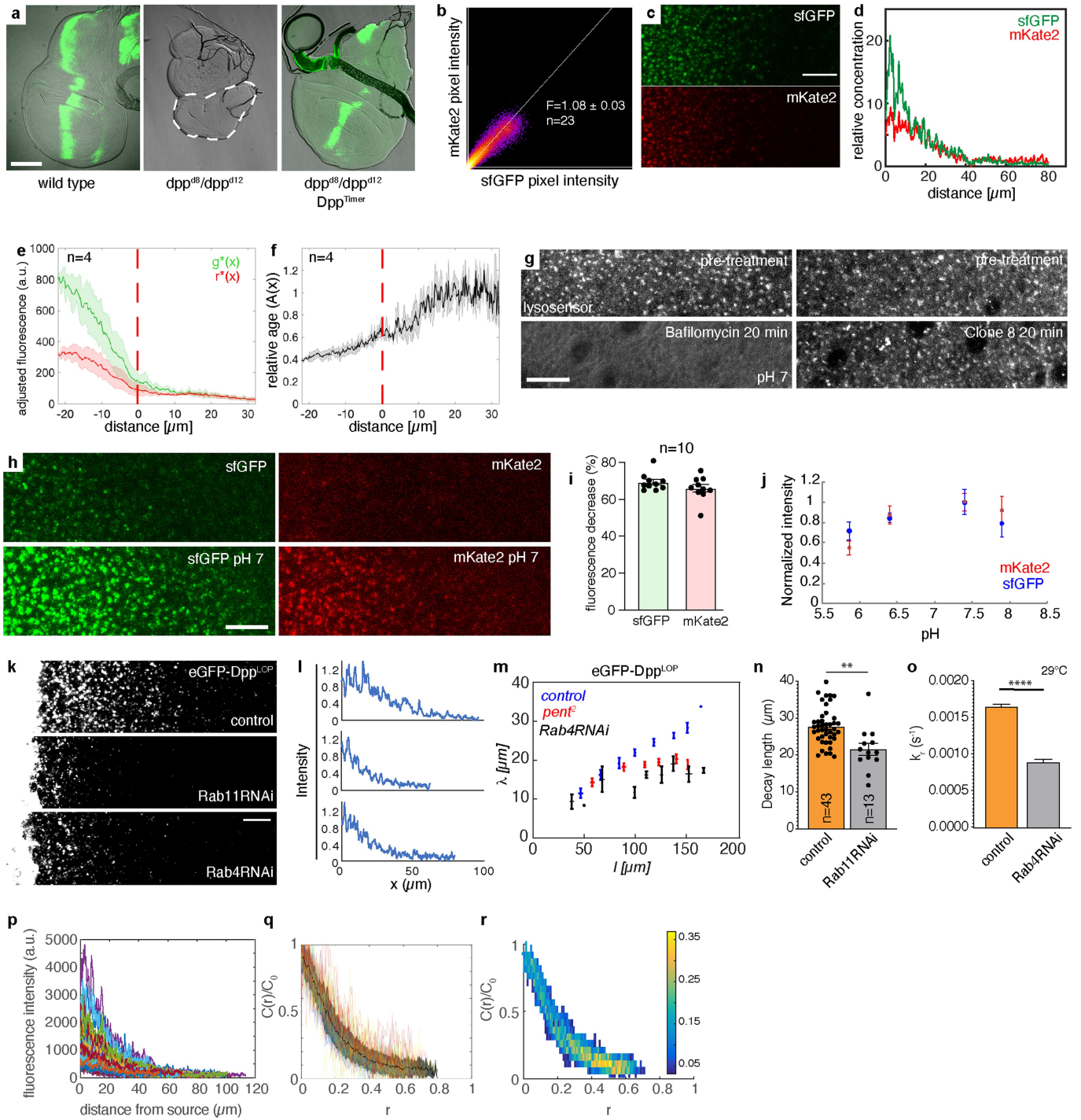
Extended Data Fig. 5 | See next page for caption.

Extended Data Fig. 5 | Quantitative considerations: robustness analysis and decay length boosts.

a, Cluster of parameter value sets in the (k_{on}, k_{off}) plane corresponding to three different ranges of R^2 to the experimental FRAP recovery for the three experimental conditions. The coefficient of determination R^2 characterizes the goodness of the fit between the FRAP data and the calculated recovery curves. Relaxing the quality of fit down to $R^2 > 0.85$ (from $R^2 > 0.93$) does not populate the lower cloud, and therefore does not affect the assignment to the ExD-type versus Combined transport regimes. Points that populate the lower cloud as in the $l = 80 \mu\text{m}$ and $pent^2$ conditions) require that $R^2 < R_{th}^2$ (see Supplementary Information section 3.7 for details). **b**, Cluster of parameter value sets in the (k_{on}, k_{off}) plane corresponding to different ranges of calculated extracellular fraction ρ for the three experimental conditions. An increase in ρ beyond ρ^* is required to shift the solutions to the “lower” cloud. The lower cloud is characteristic of the ExD-type regime. **c, d**, Sets of parameter values (clouds of points) compatible with all the assays considered in this report in the (k_{on}, k_{off}) plane. Isolines for Boost k_r (**c**) and Boost k_{off} (**d**) are also represented (see look up table). See Supplementary Information section 3.5 for definition of the Boosts. The three conditions considered in this work are shown: large discs (average posterior length $l = 144 \mu\text{m}$ in the dataset; left), small discs (average $l = 80 \mu\text{m}$; centre) and $pent^2$ discs (right). **e**, Average calculated Boost k_r , Boost k_{off} and Boost D_0 for the three experimental conditions

compared to the calculated Boosts for the theoretical values of parameters in the ExD and Tr regimes. N, number of parameterized sets of values. Data represented as mean values over N parameterized value sets. Bars, s.e.m. **f-i**, iFRAP assay. **f**, Scheme of the iFRAP assay (see Supplementary Information section 2.7). **g, h**, Test of efficiency of the acid wash in the iFRAP (and photoconversion) experiment: GFP-Dpp expressing discs have been incubated in GBP-Alexa555 for 50 min at 4 °C (the nanobody is only bound to the extracellular pool) and subsequently acid-washed to remove the label of the extracellular pool. Confocal image of eGFP-Dpp^{LOP} expressing disc (**g**) and corresponding images of GBP-Alexa555 (**h**) at indicated times after the acid wash (see Materials and Methods). Note that no detectable GBP-Alexa555 signal is observed 40 min after the acid wash, indicating that the extracellular pool of nanobodies has been efficiently removed and that the potential extracellular leftover (below the detection limit) cannot lead to an observable recovery in intracellular compartments. **i**, Theoretical dynamics of GBP-Alexa555 fluorescence recovery in the iFRAP experiment normalized to the pre-photobleaching levels. Recovery was calculated numerically using the set of values determined experimentally for large (top) and small discs (bottom). The dashed lines indicate the estimated fraction of recovery 2,000s after photobleaching in large and small discs to compare with the experimental conditions in the iFRAP experiments (Fig. 4g). Scale bar, 10 μm (**g, h**).

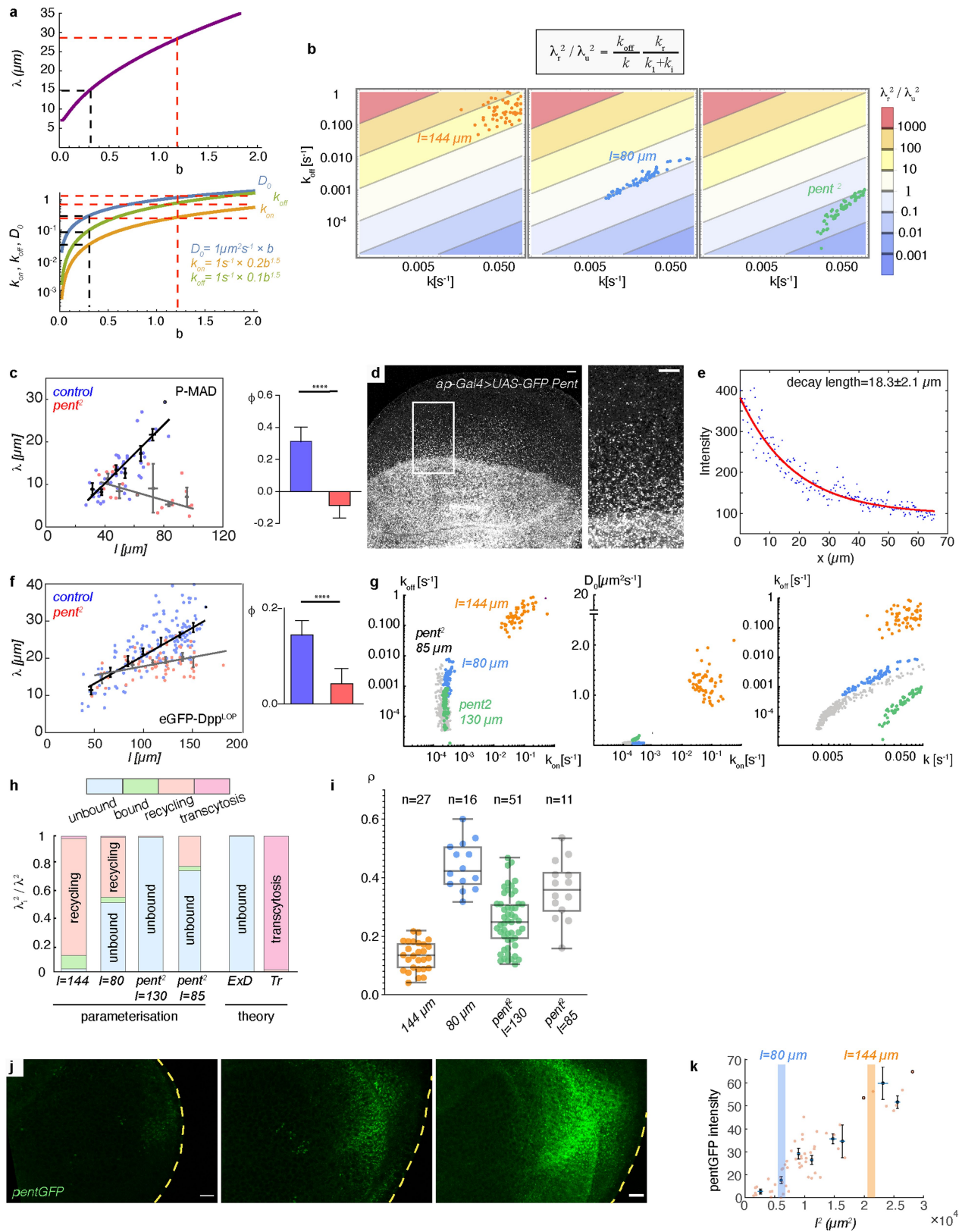
Article



Extended Data Fig. 6 | See next page for caption.

Extended Data Fig. 6 | Internalized Dpp is recycled and spreads in the tissue: Dpp^{Timer} and recycling Rab proteins. **a**, Functionality of Dpp^{Timer}. Left, control disc, expressing sfGFP-mKate2-Dpp under the control of the GAL4/UAS expression system (Dpp^{Timer}). Centre, *dpp* mutant disc, the wing imaginal disc is outlined with the white dashed line. Right, *dpp* mutant disc expressing Dpp^{Timer}. Note that the mutant phenotype seen in the central image is rescued. **b**, Scatter plot of sfGFP and mKate2 pixel intensities and linear fit to obtain the calibration factor F (see Supplementary Information section 2.6.3). $n = 23$ beads. **c**, Confocal images of the Dpp^{Timer} gradient in the wing disc (sfGFP, top and mKate2, bottom). **d**, Relative concentration profiles of mature sfGFP and mKate2 plotted against the distance from the Dpp source (see Supplementary Information section 2.6.3), corresponding to the intensity profiles measured from the images in **c**. These intensity profiles represent the relative amounts of sfGFP and mature mKate2 molecules. **e**, Adjusted fluorescence intensity profiles for sfGFP ($g'(x)$) and mature mKate2 ($r'(x)$) which are proportional to the respective concentration profiles. X-axis represents the distance from the source. Red dashed line is positioned at the anterior-posterior boundary. Note that both in the source and in the region of the target closer to the source, there are less mature mKate2 molecules, confirming that Dpp molecules are younger closer to the source. **f**, Plotted relative age ($A(x)$) of Dpp molecules as a function of position calculated from the calibrated profiles in **e**. Note that as molecules move away from the source they become older on average: $A(x)$ increases and plateaus at values close to 1. n , number of biologically independent samples. Shaded areas, s.e.m. (**e**, **f**). **g-j**, Effect of pH on the Timer. **g**, Control of the bafilomycin treatment. Confocal images of a ROI in discs incubated with a LysoSensorTM probe for 30 min before (top) and after (bottom) incubation in control Clone 8 medium (right) or bafilomycin solution (left). **h**, Effect of pH on sfGFP and mKate2 in the Dpp^{Timer}. Confocal images of sfGFP (left) and mKate2 (right) of Dpp^{Timer} before (top) and after (bottom) neutralization of pH to 7 following bafilomycin treatment for 30 min. **i**, Fluorescence signal decrease of sfGFP and mKate2 owing to acidic pH in intracellular compartments. Percentage decrease of fluorescence from pH 7 (discs after bafilomycin treatment) to the acidic environment in intracellular compartments (discs

before bafilomycin treatment). Note that the decrease is very similar for both fluorophores. **j**, Normalized fluorescence intensity of sfGFP (blue) and mKate2 (orange) in purified Timer molecules in solutions at different pH. Data normalized to the intensity at pH 7.4. The number of biologically independent samples for this analysis: $n_{\text{pH}5.86} = 8$; $n_{\text{pH}6.4} = 7$; $n_{\text{pH}7.4} = 7$; $n_{\text{pH}7.9} = 5$. Data represented as mean values \pm s.e.m. Note, that the difference between the normalized intensity of sfGFP and mKate2 at the different pH value is not significant (p -value > 0.05 ; two-tailed two sample t-test). **k**, Confocal images of eGFP-Dpp^{LOP} in control condition (top) and after RNAi through expression of dsRNA for the recycling Rab proteins, Rab11 (middle) and Rab4 (bottom) in posterior target cells. **l**, Spatial fluorescence profiles of eGFP-Dpp^{LOP} corresponding to control (top), Rab11RNAi (middle) and Rab4RNAi (bottom) conditions in **k**. **m**, Decay length λ of eGFP-Dpp^{LOP} gradient versus posterior compartment length l for control ($n = 157$), *pent*² discs ($n = 63$) and Rab4RNAi ($n = 39$). Dots, binned data; bars, s.e.m. Control and *pent*² data as in Fig. 2a, Extended Data Fig. 7f. **n**, Average eGFP-Dpp^{LOP} decay length in control and Rab11RNAi conditions. Difference between the two conditions is significant as determined by a two-tailed, two sample t-test with unequal variances, p -value = 0.0034. **o**, Recycling rate in control and Rab4RNAi conditions, determined by the nanobody uptake assay. Number of curves for each condition is $n = 4$. Difference between the two conditions is significant; two-tailed, two sample t-test with unequal variances, p -value < 0.0001 . Rab4RNAi expression was driven by means of the thermosensitive Gal4Gal80^{ts} system (29 °C). **p-r**, Scaling of eGFP-Dpp^{LOP}. **p**, Dpp gradient profiles of discs from 40 to 160 μm posterior length. Each individual profile was fitted to an exponential function with an offset (see Supplementary Information section 2.1.2) and the offset returned from the fit was subtracted. **q**, Normalized Dpp gradient profiles. Each profile was normalized to the amplitude C_0 of its exponential fit in the ordinates ($C(r)/C_0$) and to the posterior length l of the corresponding wing disc in the abscissas ($r=x/l$). Shaded area, s.e.m. Black line, average normalized profile. **r**, Density plot of **q**: Colour-code corresponds to the fraction of the number of gradients passing through a certain r , $C(r)/C_0$ bin. Scale bars, 100 μm (**a**) and 10 μm (**c**, **g**, **h**, **k**).

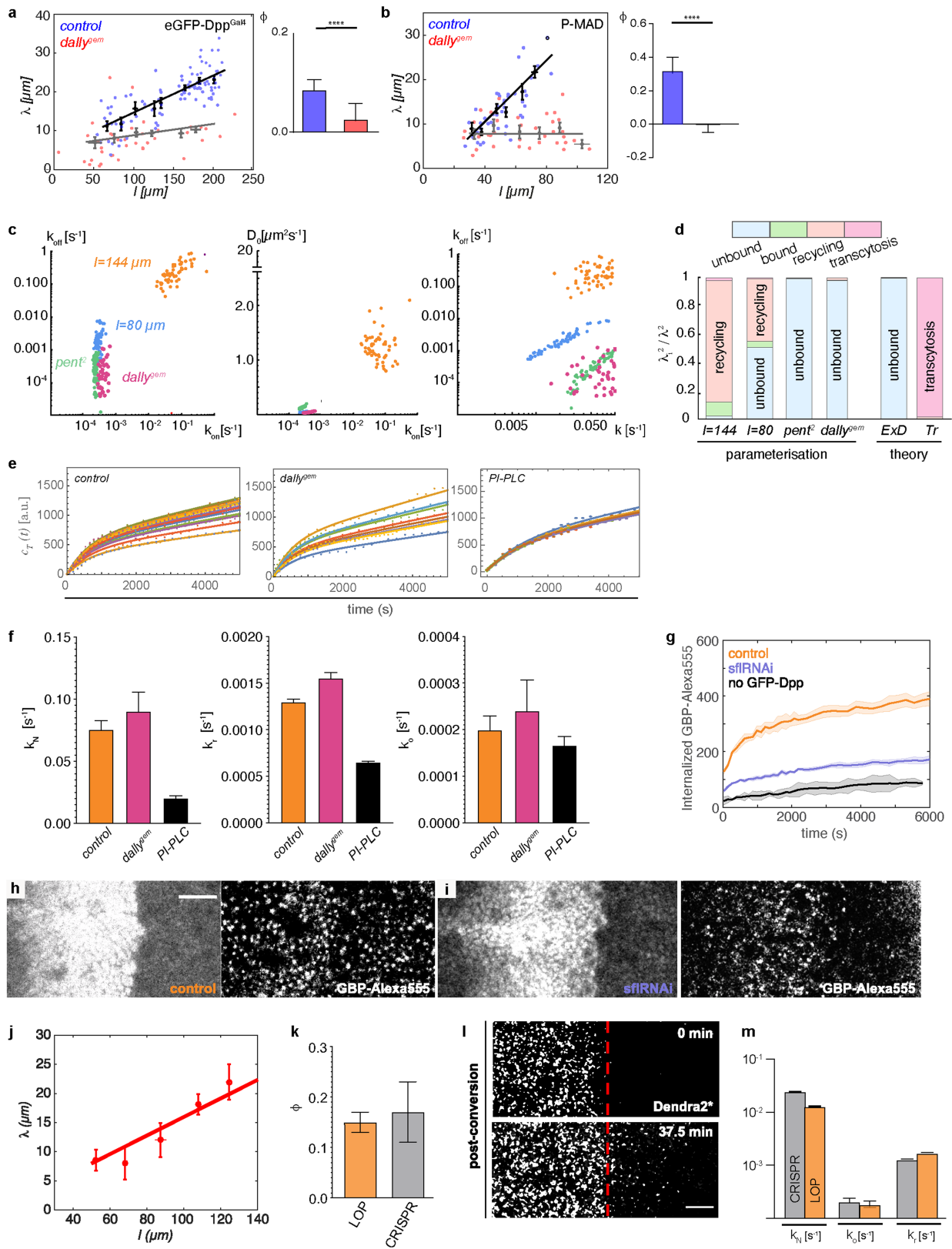


Extended Data Fig. 7 | See next page for caption.

Extended Data Fig. 7 | Gradient scaling by recycling: Pentagone.

a, Continuous and monotonic transition from $\lambda \approx 15 \mu\text{m}$ (black dashed line) to $\lambda \approx 27 \mu\text{m}$ (red dashed line). Left: decay length (λ) versus a parameter b that captures monotonic and continuous changes in k_{on} , k_{off} and D_0 as shown in the right. Right: Variations in k_{on} , k_{off} and D_0 with b as defined by the equations shown in the plot. Black and red dashed lines indicate initial (small discs) and final (large discs) values for k_{on} , k_{off} and D_0 . **b**, Top: expression for the ratio of the recycling to the unbound module (λ_r^2/λ_u^2 , see Fig. 1c). Bottom: Sets of parameter values (clouds of points) compatible with all the assays considered in this report in the $(k_{\text{on}}, k_{\text{off}})$ plane. Isolines for $(\lambda_r^2/\lambda_u^2)$ are also shown (see look-up table). The three conditions considered in this work are shown: large discs (average posterior length $l = 144 \mu\text{m}$ in the dataset; left), small discs (average $l = 80 \mu\text{m}$; centre) and *pent*² discs (right). These isolines convey the relative importance of the recycling and the unbound modules to the Dpp transport. **c**, PMAD scaling analysis for control and *pentagone* mutants. Left, Decay length λ of PMad gradients plotted as a function of posterior compartment length l . Raw and binned data (Bar, s.e.m) are shown together with a linear regression to the raw data. Right, bar plots showing the slopes ϕ of corresponding linear regressions for control (blue) and *pentagone* mutant experimental conditions (red). Number of biologically independent samples: $n = 45$ (control) and $n = 25$ (*pent*²). ****p-value < 0.00001 ; two-tailed two sample t-test with unequal variances. Bars, confidence intervals at 95%. **d**, UAS-GFP-Pentagone expression driven by ap-Gal4. In the right, higher magnification of the area boxed in the image to the left. Scale bars, $10 \mu\text{m}$. **e**, GFP-Pentagone gradient profile in the ventral compartment. The profile is fitted to an exponential function (red) to determine the decay length shown. x , distance from the dorso-ventral

boundary. **f**, eGFP-Dpp^{LOP} scaling analysis for control and *pentagone* mutants. Left, Decay length λ of eGFP-Dpp gradients plotted as a function of posterior compartment length l . Raw and binned data (Bar, s.e.m) are shown together with a linear regression to the raw data. Right, bar plot showing the slopes ϕ of corresponding linear regressions from these plots. Control experimental condition (blue) compared to *pentagone* mutant experimental condition (red). Number of biologically independent samples: $n = 157$ (control) and $n = 63$ (*pent*²). ****p-value < 0.00001 ; two-tailed two sample t-test with unequal variances. Bars, confidence intervals at 95%. **g**, Sets of parameter values satisfying the constraints given by all the experimental assays represented in $(k_{\text{on}}, k_{\text{off}})$, (k_{on}, D_0) and (k, k_{off}) planes in the four experimental conditions: eGFP-Dpp^{LOP}-expressing discs of $144 \mu\text{m}$ and $80 \mu\text{m}$ average posterior length and *pent*² mutant discs of $130 \mu\text{m}$ and $85 \mu\text{m}$ average posterior length. **h**, Stacked bar chart showing the relative contribution of the different modules to λ^2 (described in Fig. 1e, f) in the four experimental conditions in **e** compared to the theoretical values of parameters in the extracellular diffusion (ExD) and transcytosis regimes of transport (Tr). **i**, Average extracellular fraction in control discs of $144 \mu\text{m}$ and $80 \mu\text{m}$ average posterior length and *pent*² mutant discs of $130 \mu\text{m}$ and $85 \mu\text{m}$ average posterior length. Box plot represents the minimum and the maximum, median, 25th and 75th percentile. n , number of biologically independent samples. **j**, Confocal images of PentGFP from the endogenous gene in discs of different sizes. Scale bar, $10 \mu\text{m}$. Dotted lines, contour of discs. **k**, PentGFP average intensity in its expression domain as a function of the squared posterior length of the wing disc; Black, binned data. Orange dots, raw data. Bars, s.e.m. Vertical boxes indicate posterior width sizes $l = 144 \mu\text{m}$ (orange) and $l = 80 \mu\text{m}$ (blue).



Extended Data Fig. 8 | See next page for caption.

Extended Data Fig. 8 | Gradient scaling by recycling: HSPGs. a, b. Scaling analysis for control and *dally* mutants. Left, decay length λ of eGFP-Dpp (a) and P_{Mad} gradients (b) plotted as a function of posterior compartment length l . Raw and binned data (bars, s.e.m.) are shown together with a linear regression to the raw data. Right, bar plots showing the slopes ϕ of corresponding linear regressions for control experimental conditions (blue) compared to *dally* mutant experimental conditions (red). Number of biologically independent samples: $n = 93$ (control) and $n = 39$ (*dally*^{gem}) (a); $n = 43$ (control) and $n = 36$ (*dally*^{gem}) (b). ****p-value < 0.00001; two-tailed two sample t-test with unequal variances. Bars, confidence intervals at 95%. c, Sets of parameter values satisfying the constraints given by all the experimental assays represented in (k_{on}, k_{off}) , (k_{on}, D_0) and (k, k_{off}) planes in the four experimental conditions: eGFP-Dpp discs of 144 μm and 80 μm average posterior length, *pent*² (average length, 130 μm) mutant and *dally*^{gem} mutant discs (average length, 174 μm). d, Stacked bar chart showing the relative contribution of the different modules to λ^2 (described in Fig. 1e,f) in the four experimental conditions compared to the theoretical values of parameters in the extracellular diffusion (ExD) and transcytosis regimes of transport (Tr). e, GBP-Alexa555 signal intensity as a function of time in discs expressing eGFP-Dpp^{Gal4} in control discs (left), *dally*^{gem} mutant discs (middle) and control discs following treatment with PI-PLC for 1h (right). Lines, fits to the phenomenological equation describing the internalized signal intensity dynamics $C_i(t)$. f, Values of k_N , k_r and k_0 estimated by the nanobody uptake assay in control discs, *dally*^{gem} mutant discs and PI-PLC treated discs expressing eGFP-Dpp^{Gal4}. g, Internalized GBP-Alexa555

fluorescence as a function of time in discs expressing eGFP-Dpp^{CRISPR} (control), discs expressing eGFP-Dpp^{CRISPR} and sfIRNAi (sfIRNAi) and control discs (no GFP-Dpp). Number of biologically independent samples: $n = 3$ for each condition. Data represented as the average curve. Shaded area, s.e.m. h, i, Confocal images of eGFP-Dpp^{CRISPR} (left) and internalized GBP-Alexa555 (right) after 85 min of incubation with the nanobody in control discs (h) and discs expressing sfIRNAi in the posterior compartment (i). Posterior compartment, to the right from the GFP-Dpp source boundary. j, Decay length of the eGFP-Dpp^{CRISPR} gradient λ as a function of the posterior compartment width l . Red line, linear regression to the raw data. bars, s.e.m. eGFP-Dpp^{CRISPR} was visualized by means of a nanobody uptake assay (Methods). Number of biologically independent samples $n = 38$. k, Slope ϕ of the linear regressions for scaling plots corresponding to eGFP-Dpp^{LOP} (LOP) and eGFP-Dpp^{CRISPR} (CRISPR). Bars, confidence intervals of the fitted slope. l, Confocal images of photoconverted GBP-Dendra2* in eGFP-Dpp^{CRISPR}-expressing discs at different times after photoconversion (post-conversion). Before photoconversion, discs were incubated in GBP-Dendra2* solution for 45 min and extracellular GBP-Dendra2 was removed by an acid wash, so that only internalized GBP-Dendra2 is remaining. PhotoconvOgradient outside of the photoconverted region. m, The values of k_N , k_r and k_0 estimated by the nanobody uptake parameters for large discs expressing eGFP-Dpp^{CRISPR} versus eGFP-Dpp^{LOP}. Bars, confidence intervals of the fits. Number of biologically independent samples $n = 10$ (eGFP-Dpp^{CRISPR}) and $n = 13$ (eGFP-Dpp^{LOP}). Scale bar, 10 μm (h, i).

Article

Extended Data Table 1 | Rates of Dpp transport

	<i>literature</i>	$\ell = 144\mu\text{m}$	$\ell = 80\mu\text{m}$	<i>pent</i> ²	<i>ExD</i>	<i>Tr</i>
D_0 [$\mu\text{m}^2\text{s}^{-1}$]	10 [29]	1.24 ± 0.27	0.042 ± 0.005	0.12 ± 0.014	20	0.001
k_{on} [s^{-1}]		0.082 ± 0.083	$(3.0 \pm 0.53) \cdot 10^{-4}$	$(2.5 \pm 0.25) \cdot 10^{-4}$	0.025	0.5
k_{off} [s^{-1}]	$1.3 \cdot 10^{-3}$ [19] BMP1AR-BMP4	0.27 ± 0.18	$(1.9 \pm 1.7) \cdot 10^{-3}$	$(3.2 \pm 2.2) \cdot 10^{-4}$	$5.4 \cdot 10^{-7}$	0.8
k [s^{-1}]	0.020 [20,21,23] <i>Clathrin endocytosis,</i> <i>EGFR</i>	0.06 ± 0.02	0.023 ± 0.016	0.058 ± 0.021	0.002	0.06
k_r [s^{-1}]	$1.1 \cdot 10^{-3}$ $1.8 \cdot 10^{-3}$ [18, 25] <i>EGF, EGFR</i>	$(1.72 \pm 0.0002) \cdot 10^{-3}$	$(2.2 \pm 0.023) \cdot 10^{-3}$	$(2.7 \pm 0.06) \cdot 10^{-3}$	$5.3 \cdot 10^{-5}$	0.75
k_o [s^{-1}]	$1.6 \cdot 10^{-5}$ $9 \cdot 10^{-4}$ [22, 24] <i>VEGF-A, Nodal</i>	$(2.0 \pm 0.35) \cdot 10^{-4}$	$(2.1 \pm 0.06) \cdot 10^{-4}$	$(3.58 \pm 0.33) \cdot 10^{-4}$	0.029	0.0015
k_1 [s^{-1}]		$(1.9 \pm 0.79) \cdot 10^{-4}$	$(1.8 \pm 0.21) \cdot 10^{-4}$	$(2.9 \pm 0.47) \cdot 10^{-4}$	0.0284	0.0005
k_i [s^{-1}]		$(1.5 \pm 0.44) \cdot 10^{-5}$	$(3.1 \pm 1.5) \cdot 10^{-5}$	$(6.4 \pm 3.3) \cdot 10^{-5}$	$6 \cdot 10^{-4}$	0.001
k_2 [s^{-1}]		$(1.6 \pm 0.45) \cdot 10^{-5}$	$(4.5 \pm 2.2) \cdot 10^{-5}$	$(2.69 \pm 1.1) \cdot 10^{-5}$	$3.2 \cdot 10^{-5}$	$4.5 \cdot 10^{-5}$

Dpp transport parameters determined using the parameterization assays and applying the approximate Bayesian computation method.

Extended Data Table 2 | Parameterization assays

	$\ell = 144\mu\text{m}$	$\ell = 80\mu\text{m}$	$pent^2$	ExD	Tr
$A [s^{-1}]$	$1.1 \pm 0.024 \cdot 10^{-3}$	$2.1 \pm 0.015 \cdot 10^{-4}$	$2.4 \pm 0.18 \cdot 10^{-3}$	$2.1 \cdot 10^{-3}$	$4.6 \cdot 10^{-5}$
B	6.79 ± 0.15	1.21 ± 0.010	8.43 ± 0.68	$1.3 \cdot 10^{-4}$	$3.1 \cdot 10^{-2}$
$p [s^{-1}]$	$1.72 \pm 0.013 \cdot 10^{-3}$	$2.4 \pm 0.023 \cdot 10^{-3}$	$2.92 \pm 0.055 \cdot 10^{-3}$	0.029	0.75
$\lambda [\mu\text{m}]$	28.13 ± 0.96	15.87 ± 0.54	20.95 ± 0.54	28	28
$\ell [\mu\text{m}]$	144.6 ± 4.0	79.3 ± 1.4	129.8 ± 4.9	144	144
ρ	0.13 ± 0.01	0.43 ± 0.02	0.25 ± 0.01	0.02	0.98
$K_{eff} [s^{-1}]$	$4.30 \pm 0.40 \cdot 10^{-4}$	11.20 $\pm 2.37 \cdot 10^{-4}$	$7.03 \pm 0.80 \cdot 10^{-4}$		
$D_{eff} [\mu\text{m}^2 \text{s}^{-1}]$	0.359 ± 0.022	0.283 ± 0.057	0.282 ± 0.024		
B_{kr}	2.98 ± 0.46	1.32 ± 0.065	1.02 ± 0.008	1	166.99
B_{koff}	11.32 ± 12.37	1.37 ± 0.08	1.02 ± 0.009	1.0001	632.22
B_{D_0}	7.99 ± 1.39	14.79 ± 1.59	101.51 ± 37.50	31745.9	1.01

Measured parameters used for Dpp transport rates estimation by the approximate Bayesian computation method.

Reporting Summary

Nature Research wishes to improve the reproducibility of the work that we publish. This form provides structure for consistency and transparency in reporting. For further information on Nature Research policies, see our [Editorial Policies](#) and the [Editorial Policy Checklist](#).

Statistics

For all statistical analyses, confirm that the following items are present in the figure legend, table legend, main text, or Methods section.

n/a Confirmed

- The exact sample size (n) for each experimental group/condition, given as a discrete number and unit of measurement
- A statement on whether measurements were taken from distinct samples or whether the same sample was measured repeatedly
- The statistical test(s) used AND whether they are one- or two-sided
Only common tests should be described solely by name; describe more complex techniques in the Methods section.
- A description of all covariates tested
- A description of any assumptions or corrections, such as tests of normality and adjustment for multiple comparisons
- A full description of the statistical parameters including central tendency (e.g. means) or other basic estimates (e.g. regression coefficient) AND variation (e.g. standard deviation) or associated estimates of uncertainty (e.g. confidence intervals)
- For null hypothesis testing, the test statistic (e.g. F , t , r) with confidence intervals, effect sizes, degrees of freedom and P value noted
Give P values as exact values whenever suitable.
- For Bayesian analysis, information on the choice of priors and Markov chain Monte Carlo settings
- For hierarchical and complex designs, identification of the appropriate level for tests and full reporting of outcomes
- Estimates of effect sizes (e.g. Cohen's d , Pearson's r), indicating how they were calculated

Our web collection on [statistics for biologists](#) contains articles on many of the points above.

Software and code

Policy information about [availability of computer code](#)

Data collection Software built in the microscopes for image acquisition. Numerical simulations were performed on code that was custom written in C++. Source codes are available in Github (<https://github.com/zenah12/DppTrafficking-/blob/main/README.md>).

Data analysis Image analysis has been performed using Image j (version 2.0.0-rc-69/1.52p). Spatial gradient analysis performed using Matlab R2019b (9.7.0.1216025). Simulated data and nanobody recovery experimental data was analyzed using Wolfram Mathematica 12.1.1.0. Also used Excel version 16.36 and Prism 9 version 9.3.0.

For manuscripts utilizing custom algorithms or software that are central to the research but not yet described in published literature, software must be made available to editors and reviewers. We strongly encourage code deposition in a community repository (e.g. GitHub). See the Nature Research [guidelines for submitting code & software](#) for further information.

Data

Policy information about [availability of data](#)

All manuscripts must include a [data availability statement](#). This statement should provide the following information, where applicable:

- Accession codes, unique identifiers, or web links for publicly available datasets
- A list of figures that have associated raw data
- A description of any restrictions on data availability

Source data are provided with this paper. Datasets generated during the parameter estimation are available in Github (<https://github.com/zenah12/DppTrafficking-/blob/main/README.md>).

Field-specific reporting

Please select the one below that is the best fit for your research. If you are not sure, read the appropriate sections before making your selection.

- Life sciences Behavioural & social sciences Ecological, evolutionary & environmental sciences

For a reference copy of the document with all sections, see [nature.com/documents/nr-reporting-summary-flat.pdf](https://www.nature.com/documents/nr-reporting-summary-flat.pdf)

Life sciences study design

All studies must disclose on these points even when the disclosure is negative.

Sample size	<p>Decay length assay, extracellular fraction assay: Sample sizes were chosen to ensure narrow confidence intervals of fitted variables (with mean/sem > 10) and a high determination coefficient value.</p> <p>Nanobody assay: we chose a sample size for the nanobody experiment that yields sem for each point in the dynamics curve that is substantially smaller than the mean measurement (with mean/sem > 10).</p> <p>FRAP: for the FRAP experiments we progressively increased the sample size until the quality of the fit to a simple FRAP recovery curve described by an effective diffusion and effective degradation no longer improved with additional samples, and similarly the estimates for the effective diffusion and degradation no longer moved when additional samples were included (see Extended Data Figure 4c,d and the supplementary information chapter 2.5 for FRAP assay).</p> <p>iFRAP assay: We used a number of samples that yield a mean recovery that was substantially smaller than the sem.</p> <p>Timer assays: We used a number of samples that yield a mean age ratio that was substantially smaller than the sem.</p> <p>The sample size for iFRAP and timer experiments were sufficient to perform the necessary statistical test and the SEM was much smaller than the mean.</p> <p>Note that the sample sizes chosen are equal or above the typical sample sizes used in the field of developmental biology. For the clones experiment in Figure 4a,b, the experiment has been performed in triplicate and a representative image has been chosen for illustration.</p>
Data exclusions	No data exclusion
Replication	For each assay and condition, experiments were replicated independently, in wing discs from different flies at the same developmental stage and of the same genetic background.
Randomization	Flies of the same genetic background were kept separate and each experiment was carried out on discs obtained from randomly chosen fly larvae of the appropriate genetic background and developmental stage. Our study does not explore the impact of different treatments on subjects, nor did it require sampling individuals that belong to different groups from large populations. As such randomization is not strictly relevant to our analysis.
Blinding	Our analysis did not involve quantifying the impact of treatments on different groups, as such blinding was not necessary. Quantification was performed using the same programming scripts for all samples. Furthermore, the quantifications in all experiments were performed at the absence of information regarding the genetic background or developmental stage of samples.

Reporting for specific materials, systems and methods

We require information from authors about some types of materials, experimental systems and methods used in many studies. Here, indicate whether each material, system or method listed is relevant to your study. If you are not sure if a list item applies to your research, read the appropriate section before selecting a response.

Materials & experimental systems

n/a	Involved in the study
<input type="checkbox"/>	<input checked="" type="checkbox"/> Antibodies
<input checked="" type="checkbox"/>	<input type="checkbox"/> Eukaryotic cell lines
<input checked="" type="checkbox"/>	<input type="checkbox"/> Palaeontology and archaeology
<input type="checkbox"/>	<input checked="" type="checkbox"/> Animals and other organisms
<input checked="" type="checkbox"/>	<input type="checkbox"/> Human research participants
<input checked="" type="checkbox"/>	<input type="checkbox"/> Clinical data
<input checked="" type="checkbox"/>	<input type="checkbox"/> Dual use research of concern

Methods

n/a	Involved in the study
<input checked="" type="checkbox"/>	<input type="checkbox"/> ChIP-seq
<input checked="" type="checkbox"/>	<input type="checkbox"/> Flow cytometry
<input checked="" type="checkbox"/>	<input type="checkbox"/> MRI-based neuroimaging

Antibodies

Antibodies used

-Drosophila Ptc (Apa 1) was deposited to the DSHB by Guerrero, I. (DSHB Hybridoma Product Drosophila Ptc (Apa 1)) .
 -Rabbit-anti-P-Mad (PS-1) (from Tanimoto H, Itoh S, ten Dijke P, Tabata T. Hedgehog creates a gradient of DPP activity in Drosophila wing imaginal discs. Mol Cell. 2000 Jan;5(1):59-71. doi: 10.1016/s1097-2765(00)80403-7. PMID: 10678169.)

Validation

-mouse-anti-GFP antibodies (Santa Cruz # sc-9996)
 -mouse-anti-GFP antibodies (clones 7.1 and 13.1) (Roche Cat. No. 11 814 460 001)

-Drosophila Ptc (Apa 1) was deposited to the DSHB by Guerrero, I. (DSHB Hybridoma Product Drosophila Ptc (Apa 1)) : verified in Drosophila embryos in Capdevila J, Pariente F, Sampedro J, Alonso JL, Guerrero I. Subcellular localization of the segment polarity protein patched suggests an interaction with the wingless reception complex in Drosophila embryos. *Development*. 1994 Apr;120(4):987-98. PMID: 7600973. Additionally verified in Drosophila wing discs in Capdevila J, Estrada MP, Sánchez-Herrero E, Guerrero I. The Drosophila segment polarity gene patched interacts with decapentaplegic in wing development. *EMBO J*. 1994 Jan 1;13(1):71-82. PMID: 8306973; PMCID: PMC394780.

-Rabbit-anti-P-Mad (PS-1) : this antibody has been verified in Drosophila wing discs to specifically detect phosphorylated MAD as indicator for Dpp signaling activity (see Tanimoto H, Itoh S, ten Dijke P, Tabata T. Hedgehog creates a gradient of DPP activity in Drosophila wing imaginal discs. *Mol Cell*. 2000 Jan;5(1):59-71. doi: 10.1016/s1097-2765(00)80403-7. PMID: 10678169.)

-mouse-anti-GFP antibodies (Santa Cruz # sc-9996) : cited in 2,892 publications, recommended for western blot and immunoprecipitation. Chosen citations: 1. Hiscox, S., et al. 2002. GPI-anchored GFP signals Ca²⁺ but is homogeneously distributed on the cell surface. *Biochem. Biophys. Res. Commun.* 293: 714-721.
 2. Ronkina, N., et al. 2015. Comparative analysis of two gene-targeting approaches challenges the tumor-suppressive role of the protein kinase MK5/PRAK. *PLoS ONE* 10: e0136138.
 3. Kim, S.H., et al. 2016. Tunable regulation of CREB DNA binding activity couples genotoxic stress response and metabolism. *Nucleic Acids Res.* 44: 9667-9680.
 4. Guo, X., et al. 2017. VCP cooperates with UBXD1 to degrade mitochondrial outer membrane protein MCL1 in model of Huntington's disease. *Biochim. Biophys. Acta* 1863: 552-559.
 5. Mahpour, A., et al. 2018. A methyl-sensitive element induces bidirectional transcription in TATA-less CpG island-associated promoters. *PLoS ONE* 13: e0205608.
 6. Sharma, M. and Subramaniam, S. 2019. Rhes travels from cell to cell and transports Huntington disease protein via TNT-like protrusion. *J. Cell Biol.* 218: 1972-1993.
 7. Kwon, Y., et al. 2020. bPix-d promotes tubulin acetylation and neurite outgrowth through a PAK/Stathmin1 signaling pathway. *PLoS ONE* 15: e0230814.
 8. Kim, B., et al. 2021. The trehalose-6-phosphate phosphatase Tps2 regulates ATG8 transcription and autophagy in *Saccharomyces cerevisiae*. *Autophagy* 17: 1013-1027.

-mouse-anti-GFP antibodies (clones 7.1 and 13.1) (Roche Cat. No. 11 814 460 001) : from supplier's website: "Anti-GFP is tested for functionality and purity relative to a reference standard to confirm the quality of each new reagent preparation. Purity: Both Anti-GFP mouse monoclonal antibodies (Clones 7.1 and 13.1) are >95% pure as determined by SDS-PAGE and ion-exchange HPLC analyses."

Chosen citations: *Nature Communications* (2021)

BRCA2 binding through a cryptic repeated motif to HSF2BP oligomers does not impact meiotic recombination

Rania Ghouil Et Al.

Nature Microbiology (2021)

CrvA and CrvB form a curvature-inducing module sufficient to induce cell-shape complexity in Gram-negative bacteria

Nicholas R. Martin Et Al.

Nature Communications (2021)

Pathogen effector recognition-dependent association of NRG1 with EDS1 and SAG101 in TNL receptor immunity

Xinhua Sun Et Al.

Proteasomal degradation of the tumour suppressor FBW7 requires branched ubiquitylation by TRIP12

Omar M. Khan Et Al.

Nature Communications (2021)

STIM-Orai1 signaling regulates fluidity of cytoplasm during membrane blebbing

Kana Aoki Et Al.

Nature Communications (2020)

Molecular variation in a functionally divergent homolog of FCA regulates flowering time in *Arabidopsis thaliana*

Yunhe Wang Et Al.

Nature Communications (2020)

CHD7 and 53BP1 regulate distinct pathways for the re-ligation of DNA double-strand breaks

Magdalena B. Rother Et Al.

Nature Structural & Molecular Biology (2020)

Atg9 is a lipid scramblase that mediates autophagosomal membrane expansion

Kazuaki Matoba Et Al.

Nature Communications (2020)

PilY1 and minor pilins form a complex priming the type IVa pilus in *Myxococcus xanthus*

Anke Treuner-Lange Et Al.

Nature Plants (2020)

ARMADILLO REPEAT ONLY proteins confine Rho GTPase signalling to polar growth sites

Ivan Kulich Et Al.

Nature Communications (2020)

TMEM16K is an interorganelle regulator of endosomal sorting

Maja Petkovic Et Al.

Nature Communications (2020)

The netrin receptor UNC-40/DCC assembles a postsynaptic scaffold and sets the synaptic content of GABAA receptors

Xin Zhou Et Al.

Nature Communications (2020)

Pan-active imidazolopiperazine antimalarials target the *Plasmodium falciparum* intracellular secretory pathway

Gregory M. LaMonte Et Al.

Nature Communications (2020)

Plant Raf-like kinases regulate the mRNA population upstream of ABA-unresponsive SnRK2 kinases under drought stress
Fumiyuki Soma Et Al.
Nature Communications (2020)
UBB pseudogene 4 encodes functional ubiquitin variants
Marie-Line Dubois Et Al.
Nature metabolism (2020)
mTORC1 directly inhibits AMPK to promote cell proliferation under nutrient stress
Naomi Ling Et Al.

Animals and other organisms

Policy information about [studies involving animals](#); [ARRIVE guidelines](#) recommended for reporting animal research

Laboratory animals	Drosophila Melanogaster. All experiments have been performed on wing discs of larvae of ages specified in the figure legends and of random sex (males and females). The genotypes used are specified in Supplementary Tables 1 and 2.
Wild animals	the study did not involve wild animals
Field-collected samples	the study did not involve samples collected from the field
Ethics oversight	no ethical approval or guidance was required

Note that full information on the approval of the study protocol must also be provided in the manuscript.